



HAL
open science

Iron isotope signature of magnetofossils and oceanic biogeochemical changes through the Middle Eocene Climatic Optimum.

Robin Havas, Jairo F. Savian, Vincent Busigny

► **To cite this version:**

Robin Havas, Jairo F. Savian, Vincent Busigny. Iron isotope signature of magnetofossils and oceanic biogeochemical changes through the Middle Eocene Climatic Optimum.. *Geochimica et Cosmochimica Acta*, 2021, 311, pp.332-352. 10.1016/j.gca.2021.07.007 . hal-03341991

HAL Id: hal-03341991

<https://hal.science/hal-03341991>

Submitted on 16 Oct 2023

HAL is a multi-disciplinary open access archive for the deposit and dissemination of scientific research documents, whether they are published or not. The documents may come from teaching and research institutions in France or abroad, or from public or private research centers.

L'archive ouverte pluridisciplinaire **HAL**, est destinée au dépôt et à la diffusion de documents scientifiques de niveau recherche, publiés ou non, émanant des établissements d'enseignement et de recherche français ou étrangers, des laboratoires publics ou privés.



Distributed under a Creative Commons Attribution - NonCommercial 4.0 International License

1 **Iron isotope signature of magnetofossils and oceanic**
2 **biogeochemical changes through the Middle Eocene**
3 **Climatic Optimum**

4
5 Robin Havas^{1,2}, Jairo F. Savian³, Vincent Busigny^{1,4*}

6
7 ¹ Université de Paris, Institut de Physique du Globe de Paris, CNRS, F-75005, Paris, France

8 ² Université de Bourgogne, Franche-Comté, UMR CNRS 6282 Biogéosciences, Dijon, France

9 ³ Departamento de Geologia, Instituto de Geociências, Universidade Federal do Rio Grande
10 do Sul, Av. Bento Gonçalves, 9500, 91501-970 Porto Alegre, Brazil

11 ⁴ Institut Universitaire de France, 75005 Paris, France

12
13
14 * Corresponding author: Robin Havas (robin.havas@gmail.com)

15
16
17
18
19
20
21
22
23
24
25
26
27 *Keywords: iron isotopes; magnetotactic bacteria; magnetofossils; MECO; hyperthermal; Fe*
28 *sequential extraction*
29

34 **Abstract**

35

36 Magnetotactic bacteria (MTB) intracellularly precipitate magnetite (Fe_3O_4) crystals that can
37 be preserved in the geological record. When MTB die, the so-called magnetofossils constitute
38 valuable proxies for paleoenvironmental reconstructions and are suspected to represent some
39 of the oldest traces of biomineralization on Earth. Yet, the biogenicity of putative
40 magnetofossils found in ancient terrestrial and extra-terrestrial samples is still largely debated
41 and their significance for past climate still holds uncertainties. Here we studied a sedimentary
42 sequence from the Indian Ocean (ODP Hole 711A) recording the Middle Eocene Climatic
43 Optimum (MECO) through which a magnetofossil-rich interval was deposited. We
44 investigated for the first time the potential of Fe isotopes as a biosignature in magnetofossils
45 and thoroughly describe MECO related paleoenvironmental disruptions based on major and
46 trace element concentrations. Bulk sediment Fe isotopes showed limited variations, with
47 $\delta^{56}\text{Fe}$ around $-0.13 \pm 0.04 \text{ ‰}$ ($n=24$), linked to detrital iron rather than MTB activity. Hence, a
48 sequential chemical extraction protocol was applied to determine the specific composition of
49 magnetite. We discuss analytical biases related to this protocol (*i.e.* partial phyllosilicate and
50 Mn-oxide leaching) and apply corrections to the data. Outside the magnetofossil-rich interval,
51 Fe isotope compositions of oxides (mainly biotic and/or abiotic magnetites and possibly Fe
52 coprecipitated with Mn-oxides) display a small range averaging $-0.54 \pm 0.05 \text{ ‰}$, and are
53 interpreted as reflecting dominantly hydrothermal contribution, a conclusion also supported
54 by prominent Eu anomaly. In contrast, the magnetofossil-rich interval shows larger $\delta^{56}\text{Fe}$
55 variability in oxides, from -0.12 to -0.94 ‰ , decreasing upwards in the stratigraphic section.
56 This interval likely records enhanced Fe supply from atmospheric fallout, increase in
57 biological productivity (illustrated by increased Ba accumulation rate) and subsequent
58 development of ferruginous conditions in the sediment porewater. Covariations of Fe isotope
59 compositions and Mn/Fe ratios can be explained by a vertical migration of a redox front and
60 associated diagenetic modifications. Precipitation of barite (BaSO_4) in the sediments after
61 organic matter decay probably favored the preservation of magnetofossils by decreasing SO_4^{2-}
62 concentration in porewaters and subsequent H_2S production, which usually dissolve magnetite
63 in the sulfidic zone. Finally, we model the evolution of porewater fluid and estimate Fe
64 isotope fractionation between magnetofossils and fluid to $\Delta^{56}\text{Fe}_{\text{mag-Fe(II)aq}} = 0.1\text{-}0.3 \text{ ‰}$, a value
65 significantly different from abiotic magnetite fractionation ($\sim 1.5 \text{ ‰}$). Contrasting with recent
66 results on MTB laboratory culture, no mass independent fractionation of Fe isotopes was

67 observed in the present study. Nevertheless, the diverse geochemical proxies presented here
68 provide important constraints on paleoclimate and magnetofossil biogenicity evaluation.

69
70

71 **1. INTRODUCTION**

72

73 The Middle Eocene Climatic Optimum (MECO) is a global warming episode (+4-6 °C; Bijl et
74 al., 2010) that cut through the Eocene long-term cooling trend about 40 Ma ago. It has been
75 interpreted as reflecting increased atmospheric $p\text{CO}_2$ (by a factor of 2 to 3) and lasted ~500
76 ka, as defined by the negative excursion observed in $\delta^{18}\text{O}$ values from worldwide marine
77 carbonates (Bohaty and Zachos, 2003; Bijl et al., 2010; Bohaty et al., 2009). The MECO
78 differs from other Paleocene and Eocene hyperthermal events by its duration and timing, and
79 because the overall carbon cycle and the origin of the event are poorly understood (Bohaty et
80 al., 2009; Sluijs et al., 2013; van der Ploeg et al., 2018; Giorgioni et al., 2019). A direct
81 consequence of increasing $p\text{CO}_2$ is an acidification of the oceans and therefore an increase of
82 carbonate dissolution through shallowing of calcite compensation depth (CCD) recorded
83 worldwide (Bohaty et al., 2009; Pälike et al., 2012). Additionally, changes in surface nutrients
84 cycling, biotic conditions, primary productivity and organic matter export have been reported
85 in many near-shore environments (Spofforth et al., 2010; Luciani et al., 2010; Toffanin et al.,
86 2010; Witkowski et al., 2012; 2014; Boscolo Galazzo et al., 2015; Moebius et al., 2014;
87 2015).

88 Similarly as for the Paleocene Eocene Thermal Maximum (PETM), sediments recording the
89 MECO have been associated to magnetofossil deposits (Chang et al., 2012; Savian et al.,
90 2014; 2016). Magnetofossils are fossilized magnetite or greigite crystals, initially precipitated
91 from magnetotactic bacteria (MTB). The magnetic crystals are organized as chains, allowing
92 MTB to orientate themselves along the Earth's magnetic field, which facilitates their search
93 for optimal conditions. These conditions correspond to low oxygen contents, at or near redox
94 boundaries, and high concentration of nutrients like iron (Bazylinski and Frankel, 2003;
95 Komeili, 2012; Lefèvre and Bazylinski, 2013). Because they are bound to such contexts of
96 formation, deposition and preservation, magnetofossils constitute important proxies for redox,
97 biogeochemical and magnetic characterization of paleoenvironments (Kopp and Kirschvink,
98 2008; Roberts, 2015). More specifically, magnetofossils have been used to trace variations in
99 paleoproductivity, oceans circulation, stratification, temperature or dissolved Fe availability

100 as well as diagenetic redox conditions or glacial/inter-glacial cycles (e.g. Hesse, 1994;
101 Dinarès-Turell et al., 2003; Kopp et al., 2007; Schumann et al., 2008; Roberts et al., 2011,
102 Roberts, 2015).

103 Promoted by natural selection, this advantage of biologically-controlled mineralization has
104 persisted through time and evolution, favoring distinctive features among MTB-biominerals
105 compared to abiogenic magnetites (Chang and Kirschvink, 1989; Kopp and Kirschvink, 2008;
106 Lin et al., 2017). In this paper, we will focus on magnetites, biologically formed greigites will
107 not be discussed further. Biomagnetites formed by MTB are characterized by (i) narrow size
108 and shape distributions, (ii) chemical purity and crystallographic perfection, (iii) presence of
109 chains, and (iv) unusual morphologies (Bazylinski and Frankel, 2003; Kopp and Kirschvink,
110 2008; Jimenez-Lopez et al., 2010; Jovane et al., 2012; Amor et al., 2020). Other features such
111 as magnetic parameters can serve for the detection of magnetites produced by MTB, notably,
112 the presence of single domain particles (Kopp and Kirschvink 2008; Savian et al. 2016; Amor
113 et al., 2020). Nevertheless, these criteria of biogenicity can be called into question and have
114 been vigorously debated for magnetites found in old Martian and terrestrial rocks (Thomas-
115 Kerpta et al., 2000; Golden et al., 2004; Jimenez-Lopez et al., 2010). Any individual criterion
116 is not sufficient by itself to meet consensus on these questions but a compilation of cross-
117 checking evidences is required. Within that framework, oxygen and iron isotopes represent
118 new possible biosignatures (Mandernack et al., 1999; Jimenez-Lopez et al., 2010; Amor et al.,
119 2016, 2018, 2020).

120 Recently, the MTB strain *Magnetospirillum magneticum* AMB-1 was shown to produce
121 magnetosomes (i.e. magnetite crystals enveloped in a lipid bilayer membrane) strongly
122 depleted in heavy iron isotopes (by ~ 2 ‰) relative to the growth medium, as well as a unique
123 mass-independent isotope fractionation on ⁵⁷Fe (Amor et al., 2016, 2018). This contrasts with
124 abiotic magnetite, which is enriched in heavy Fe isotope by ~1.5‰ and with no isotopic
125 anomaly (Johnson et al., 2005; Frierdich et al., 2014). The MTB strains MS-1 and MV-1
126 produced magnetites with temperature dependent fractionation of oxygen isotopes but
127 different from abiotic magnetite (Mandernack et al., 1999). Besides providing additional
128 criteria for biogenicity determination, isotope analyses of magnetite represent more
129 quantitative evidences and are potentially less affected by diagenesis and early metamorphism
130 than morphological and physical criteria (Vali and Kirschvink, 1989; Amor et al., 2020). Iron
131 isotopes have been used in previous studies to deduce the presence of Fe(III)-reducing and/or
132 Fe(II)-oxidizing metabolisms in the Precambrian (Archer and Vance, 2006; Johnson et al.

133 2008a; Planavsky et al., 2009; Marin-Carbonne et al., 2020) and may be a valuable tool for
134 the search of MTB in the rock record. Moreover, it can be applied to reconstruct paleo-
135 environmental modifications (*e.g.* Rouxel et al., 2005; Planavsky et al., 2009; Kurzweil et al.,
136 2016; Eickmann et al., 2018; Heard and Dauphas, 2020) and distinguish them from diagenetic
137 effects related to sediment burial (Marin-Carbonne et al., 2014).

138 The occurrence of magnetofossils in relation with sediments recording an extreme
139 paleoclimate event (*i.e.* the MECO) represents a great opportunity to investigate both
140 magnetofossil geochemical signatures as biogenicity criteria and related paleoenvironmental
141 changes. While the magnetic response to hyperthermal events like the MECO (*i.e.* increase of
142 conventional and “giant” magnetofossils deposition due to environmental changes) has been
143 widely documented (Kopp et al., 2007; Lippert and Zachos, 2007; Schumann et al., 2008;
144 Chang et al., 2012; Savian et al., 2014, 2016), geochemical characterization of MECO
145 sediments beyond carbon and oxygen isotopes is sparse (Spofforth et al., 2010).

146 In the present contribution, we studied for the first time the isotopic and geochemical
147 signatures of magnetofossils in ancient sediments. Besides, we thoroughly describe the
148 biogeochemical disruptions occurring in the Indian Ocean during the MECO. Iron isotopes
149 and major and trace element concentrations were analyzed on both bulk sediments and
150 specific fractions from sequential chemical extractions. Because chemical extraction
151 procedures may induce some analytical biases (*e.g.* Oonk et al., 2017; Slotznick et al., 2020),
152 we first discuss the reliability of our method and potential contaminations and apply
153 numerical corrections to determine magnetite geochemical signature. Then, the results are
154 used to characterize Fe biogeochemical cycle in the Indian Ocean during the MECO and
155 examine MTB biosignatures and magnetofossils preservation in the sedimentary record.
156 Finally, we discuss the data in terms of paleoenvironmental implications stemming from this
157 climatic event.

158

159

160 **2. GEOLOGICAL SETTINGS AND SAMPLES**

161

162 The samples investigated in the present work are pelagic marine sediments recovered from
163 Ocean Drilling Program (ODP) Hole 711A (Fig. 1), Madingley rise, Western Indian Ocean
164 (Leg 115 - 2°44.56'S, 61°09.78'E). Site 711A lies at a water depth of ~ 4450 m about 700 km
165 away from the central Indian ridge, Carlsberg ridge and Seychelles Plateau (Backman et al.,

166 1988). Retrieved sediments from ODP Hole 711A span a total period of ~ 45 Ma. The studied
167 interval encompasses the MECO event (about 40 Ma ago), ranging from 188.5 to 180 meters
168 below seafloor (mbsf; cores 20X and 19X, ~120 meters above the basaltic basement). It was
169 deposited at a paleodepth below 3000 m in equatorial paleolatitudes, close to the spreading
170 central Indian ridge, between the Indian and African plates (Fig. 1; Simmons, 1990; Bohaty et
171 al., 2009; Savian et al., 2013; Fioroni et al., 2015). A total of 31 samples, regularly spaced
172 (10-40 cm) through the Hole 711A drill core material, was analyzed. The sediments are
173 composed mainly of clayey/clay-bearing nannofossils chalks and clay-bearing radiolarian
174 oozes (Fig. 2A; Backman et al., 1988). A change in mineralogy from calcareous to siliceous
175 reflects a drop in the CaCO₃ mass accumulation rate (MAR) that would have resulted from an
176 acidification of the oceans during the MECO (Bohaty et al., 2009). In our samples, this
177 dramatic change in mineralogy is illustrated by CaCO₃ concentrations ranging from about 0.5
178 to 90 wt % (Fig. 2B). Magnetic characterization of Hole 711A sediments has been performed
179 and interpreted as an enrichment in magnetofossils from ~187 to 184 mbsf (Savian et al.,
180 2016). Transmission electron microscope (TEM) images of magnetofossils from ODP Hole
181 711A have been reported in previous studies (*e.g.* Fig. 2 in Chang et al., 2012; Fig. 6 in
182 Savian et al., 2016). The well-constrained transition from magnetofossils-poor to
183 magnetofossils-rich sediments, and reverse, is ideal for (1) testing iron isotopes as a potential
184 biosignature for MTB and (2) investigating the link between environmental changes and MTB
185 abundance and preservation. For this purpose, we define and discuss thereafter three distinct
186 stratigraphic intervals: the magnetofossil-poor sediments from 188.49 to 187.1 and from 184
187 to 180 mbsf referred to as zones MP1 and MP2, respectively, and the magnetofossil-rich
188 sediments from 187.1 to 184 mbsf as zone MR (Fig. 2 and 4). Following this notation, the
189 start of MR zone represents the MECO at its peak (Savian et al., 2013; Fioroni et al., 2015),
190 though a precise definition of the event's timing would require a more profound cyclo-,
191 magneto-stratigraphic and astrochronological study of the core.

192

193

194 **3. ANALYTICAL METHODS**

195

196 The chemical and isotopic compositions of bulk sediments and several mineralogical fractions
197 were determined to understand the magnetite formation mechanisms at Hole 711A, but also
198 the sediments and geological context in which they formed. Thus, a sequential extraction

199 protocol was applied to recover the different Fe-bearing phases present in our samples and
200 notably magnetite (Bayon et al., 2002; Poulton and Canfield, 2005; Henkel et al., 2016). In
201 order to adapt this protocol to our samples, we examined their mineralogy based on X-ray
202 diffraction (XRD) and scanning electron microscopy (SEM) techniques as well as previous
203 magnetic and microscopic studies about Hole 711A (Backman et al., 1988; Hempel and
204 Bohrmann, 1990; Savian et al., 2016).

205

206 **3.1. Mineralogical analyses**

207

208 X-Ray Diffraction (XRD) analyses were performed throughout the sedimentary sequence on
209 crushed bulk and calcite-free (after 10 % acetic acid dissolution) powdered samples. Samples
210 were grounded in an agate mortar (before and after acetic acid step), and deposited on a flat
211 aluminum sample holder. The XRD measurements were carried out at University of Paris
212 using a Panalytical Empyrean diffractometer equipped with a Cu anode and a multichannel
213 X'celerator detector. Mineral identification was performed using the Highscore Plus 3.0
214 software and two databases: ICSD (Inorganic Crystal Structure Database) and COD
215 (Crystallography Open Database). All quantifications were done in “semi-quantification”
216 mode, thus only providing rough relative estimates of the phase proportions.

217 Scanning electron microscopy (SEM) in back-scattered electron and secondary electron
218 imaging modes were used to characterize the shape and chemical composition of our samples.
219 Analyses were carried out in the electron microscopy platform at Institut de Physique du
220 Globe de Paris (IPGP) using a Carl Zeiss EVO MA10 SEM. Standard operating conditions
221 for SEM imaging and EDS analyses were 15 kV accelerating voltage, working distance of 12
222 mm, and electron beam current of 2-3 nA. Samples were coated with a few nanometers of Au
223 prior to analysis.

224

225 **3.2. Bulk sample digestion and sequential extraction protocol**

226

227 For bulk analyses, about 50 mg powdered samples were digested in 10 mL Teflon beakers
228 following sequences of addition, heating and evaporation of concentrated HF-HNO₃-HCl
229 acids (Table S1; Dauphas et al., 2009).

230 Sequential extraction procedures have been developed and modified for more efficiency since
231 the 60s, and are routinely applied in laboratories although they are not entirely selective phase
232 dissolution (Henkel et al., 2016 and references therein). It is important to optimize the applied

233 method and be aware of potential analytical biases (Tessier and Campbell, 1988; Nirel and
234 Morel, 1990; Slotznick et al., 2020). Because the mineralogy of our samples is quite
235 straightforward with regard to Fe-minerals, we selected and applied protocol steps from
236 previous studies targeting phases of interest (Bayon et al., 2002; Poulton and Canfield, 2005;
237 Henkel et al., 2016). Between 100 and 450 mg of the powdered samples were loaded in
238 Falcon® tubes for centrifugation at the end of each step of sequential dissolution. Leachates
239 solutions were filtered (pore diameter of 0.45 µm) for further chemical treatment. Residual
240 fractions were rinsed and agitated with deionized water (that was centrifuged/poured out) and
241 dried before further treatment.

242 *Calcium carbonate* (calcite) made up to ~ 90 wt % of some of our samples and was the first
243 targeted phase. They were removed by reacting with 10% acetic acid (shown to have little to
244 no effect on magnetite while quantitatively dissolving calcium carbonates; Bayon et al., 2002)
245 for 4h in an ultrasonic bath (~10 mL of solution for 100 mg of sample; Bayon et al., 2002;
246 Kryc et al., 2003). Leachate solutions were dried and dissolved in 0.3 M HNO₃ for major and
247 trace elements analysis.

248 *Magnetite* was the major non-silicate Fe-bearing phase (see *Results*). Hence, no Fe-
249 (oxyhydr)oxide extraction was carried out and magnetite was extracted directly after calcite
250 via a 0.2 M ammonium oxalate + 0.17 M oxalic acid solution (OA-AO; McKeague and Day,
251 1966; Kostka and Luther, 1994; Poulton and Canfield, 2005; Henkel et al., 2016). 60 mg of
252 ascorbic acid was added to the solution before reaction with the sample for quantitative
253 reduction and dissolution of magnetite. The pH of the acid oxalate solution is 2.1, which is in
254 the low range of values proposed in the literature, but only minor differences have been found
255 when changing pH from 2 to 3 (McKeague and Day, 1966). OA-AO extracts were
256 subsequently oxidized (from Fe(II) to Fe(III)) with nitric and perchloric acid at 120°C,
257 evaporated and then dissolved in 1M HNO₃ for major and trace element measurements and Fe
258 isotope chemistry. Prior to column chromatography for Fe isotope measurement, Fe was
259 precipitated and separated from the matrix using NH₄OH, following the method described by
260 Henkel et al. (2016). This precipitation step is required when leachate solutions are prepared
261 for subsequent isotopic analysis. It prevents from mass bias effects during isotope
262 measurements due to overwhelming concentrations of salts in solutions. We verified that the
263 procedure did not fractionate Fe isotopes by measuring the isotope composition of an internal
264 standard (pure iron solution) mixed with the different reactants of the protocol and then
265 processed through chemistry (Fe-precipitation and column chromatography). Six replicate
266 analyses demonstrated that the standard was identical to its accepted values within uncertainty

267 ($\pm 0.02\%$ for $\delta^{56}\text{Fe}$ values and $\pm 0.04\%$ for $\delta^{57}\text{Fe}$ values). All Fe isotope measurements from
268 oxalate fractions were duplicated (including full chemical processing).
269 Finally, after magnetite extraction, silicates and pyrite would be the remaining Fe-bearing
270 phases to extract (e.g Poulton and Canfield, 2005). However, pyrite was absent or minor in
271 our samples (see *Results*). The insoluble *residual fraction* (thereafter referred to as 'HF
272 fraction') was fully dissolved in concentrated HF-HCl-HNO₃ mixtures.

273
274

275 **3.3. Major and trace element measurements**

276
277 Major and trace element concentrations were measured on bulk samples and chemical
278 extracts. All samples were dissolved and diluted by a factor of 250-500 in 0.3 M HNO₃ for
279 analysis. Elemental concentrations were assessed using an Agilent 7900 quadrupole ICP-MS
280 at IPGP. Elements with masses between that of sodium (23) and arsenic (75) were measured
281 using a collision-reaction cell with helium gas (5mL/min) to remove polyatomic interferences.
282 All other elements were measured without collision gas. Scandium, indium and rhenium
283 internal standards were injected after inline mixing with the samples to correct for signal drift
284 and matrix effects. The reported uncertainties were calculated using the algebraic propagation
285 of blank subtraction and sample count standard deviations (n=3) and are negligible if not
286 specified.

287

288 **3.4. Iron isotope analysis**

289
290 Chemical separation of Fe from the matrix was achieved on bulk samples and chemical
291 extracts by column chromatography using an AG1-X8 200-400 mesh anion-exchange resin
292 and HCl medium (for details, see Table S1; Dauphas et al., 2004). The complete procedure of
293 Fe separation was always repeated twice for a better purification, although it might slightly
294 reduce the purification yield (83% on average bulk samples). Extracted Fe was dissolved in
295 2% HNO₃ for subsequent MC-ICP-MS analysis.

296

297 Iron isotope measurements were carried out at IPGP on a Neptune+ ThermoFinnigan MC-
298 ICP-MS. We used a stable introduction system (SIS) and the high-resolution mode to avoid
299 polyatomic argon interferences (Weyer and Schwieters, 2003). The four stable Fe isotopes
300 (masses 54, 56, 57 and 58) were measured simultaneously in order to evaluate potential mass-

301 independent fractionations (MIF), and ^{52}Cr and ^{60}Ni concentrations were monitored to correct
302 for potential contamination of ^{54}Cr and ^{58}Ni on ^{54}Fe and ^{58}Fe respectively (Schönberg and van
303 Blanckenburg, 2005).

304

305 For correction of instrumental mass fractionation, a standard-sample bracketing method
306 (SSB) was used (Belshaw et al., 2000; Schönberg and van Blanckenburg, 2005). The Fe
307 isotope composition was expressed in per mil as:

308

$$309 \quad \delta^x\text{Fe} = \left(\frac{{}^x\text{Fe}/{}^{54}\text{Fe}_{\text{sample}}}{{}^x\text{Fe}/{}^{54}\text{Fe}_{\text{standard}}} - 1 \right) \times 1000 \text{ (‰)} \quad (1)$$

310 where x states for 56, 57 or 58, and the standard is IRMM-014, a synthetic metallic iron from
311 Institut for Reference Materials and Measurements (Taylor and McLennan, 1995), with
312 chondritic composition (Dauphas et al., 2009). Mass independent fractionation were evaluated
313 from the capital delta notation expressed as:

$$314 \quad \Delta^{57}\text{Fe} = \delta^{57}\text{Fe} - 1000 \times \left((1 + \delta^{56}\text{Fe}/1000)^{\beta^{57}} - 1 \right) \text{ (‰)} \quad (2)$$

315 β_{57} corresponds to the variation of $^{57}\text{Fe}/^{54}\text{Fe}$ and $^{56}\text{Fe}/^{54}\text{Fe}$ mass ratios (*i.e.* 1.475) (Young et
316 al., 2002; Amor et al., 2016).

317

318 Through all MC-ICP-MS sessions of the present study, external reproducibility (2σ interval),
319 including weighing, chemical dissolution and Fe extraction, on granite geostandard AC-E was
320 ± 0.02 and ± 0.04 ‰ for $\delta^{56}\text{Fe}$ and $\delta^{57}\text{Fe}$ (n=4), respectively. External reproducibility (2σ
321 interval) on our internal standard ISVB including reaction with the extracting solvents, Fe-
322 precipitation and chemical extraction was ± 0.03 ‰ for both $\delta^{56}\text{Fe}$ and $\delta^{57}\text{Fe}$ (n=6). Analytical
323 blanks represented at most 0.8% of Fe in the oxalate fraction and less than 0.1% for bulk and
324 HF fraction samples.

325

326 **4. RESULTS**

327

328 **4.1. Mineralogy of the sediments from Hole 711A**

329

330 In samples from MP1 and MP2 zones, XRD analyses confirmed the overwhelming presence
331 of calcite followed by halite (Fig. S1). Diffractograms from MR zone sediments also showed
332 halite peaks but exhibited broader, poorly-defined peaks indicative of amorphous phases,
333 likely corresponding to radiolarian ooze observed in SEM (Backman et al, 1988; Hempel and

334 Bohrmann, 1990). Phase quantification and minor phases identification was inaccurate due to
335 the presence of this amorphous opal material but XRD analyses still allowed for identification
336 of major phases in carbonate-free sediments (see supplementary material). Through the whole
337 section, they were composed mostly of opal, clays (smectites), barite and crystalline SiO₂
338 (detrital and authigenic quartz) as well as zeolite. Sample '187.02', at the start of MR zone,
339 contains substantial clinoptilolite (also reported by Hempel and Bohrmann, 1990), which is a
340 zeolite type. Magnetite XRD peaks overlap those of smectite and were thus difficult to assess
341 in most samples (with the possible exception of sample '187.02 mbsf'; see supplementary
342 material, Fig. S2). However, magnetite crystals clearly dominate the magnetic signals of our
343 samples and have been evidenced through TEM images (Chang et al., 2012; Savian et al.,
344 2016). Ferrihydrite, goethite and hematite as well as pyrite were not detectable from XRD
345 diffractograms. SEM confirmed the presence of phases detected in XRD and put light on two
346 distinct Fe-rich and Fe-depleted aluminosilicate phases, attributed to the aforementioned clay
347 and zeolite, respectively (Fig. S3).

348

349 **4.2. Major and trace element geochemistry**

350

351 *4.2.1. Bulk analyses*

352

353 Most changes in major and trace element abundances occur concomitantly with the
354 stratigraphic shifts from calcareous to siliceous and reverse, at depths of ~ 187 and 184 mbsf
355 respectively. CaCO₃ content is about 90 wt % in MP1 and MP2 zones, and drops to ~ 0.5 wt
356 % in MR zone (Fig. 2). In contrast, Fe concentration exhibits a sharp increase at the start of
357 MR zone, from ~ 0.5 to 5.4 wt %, then averaging 1.7 wt % in the rest of this zone and
358 decreasing to ~0.8 wt % in MP2 zone (Fig. 2, Table 1). Barium increases from about 0.1 to
359 0.5 wt % (on average) between zones MP1/MP2 and MR, respectively, with a maximum
360 value of 1.2 wt % at 186.91 mbsf (Table 1). Aluminum as well as most other elements depict
361 similar trends. However, this mostly reflects variable dilution effects in carbonate-rich
362 (MP1/MP2 zones) and carbonate-poor sediments (MR zone, Fig. 3). A normalization of major
363 and trace element content to a detrital element such as Al or Zr enables to avoid this dilution
364 effect and to recognize variations of an element that are not linked to detrital sources (*e.g.*
365 Calvert and Pedersen, 1993). Unlike Fe concentrations, Fe/Al molar ratios only slightly
366 increase towards the top profile (Fig. 2). They average 0.63 ± 0.07 (n=29), close to the detrital
367 Fe/Al ratio of the HF fraction (0.59 ± 0.10 , n=17). Moreover, bulk Fe concentrations are

368 correlated to those of Al (Fig. 3) and are thus driven at first order by detrital phases through
369 the stratigraphic sequence.

370

371 Bulk samples show REE+Y patterns (rare earth elements + yttrium) with both negative
372 cerium anomaly (Ce^*) and positive europium anomaly (Eu^*). Eu^* is defined as $Eu_{SN} /$
373 $(0.66 \times Sm_{SN} + 0.33 \times Tb_{SN})$ where 'SN' stands for 'shale normalized' (Taylor and McLennan,
374 1995). For Eu^* calculation, we use 'Tb' rather than 'Gd' because seawater can have a slight
375 positive Gd anomaly (Planavsky et al., 2010) and thus hinder a possible Eu^* . Ce^* is defined
376 as $Ce_{SN} / (0.5 \times La_{SN} + 0.5 \times Pr_{SN})$ but we also use Pr anomaly (Pr^*) to decipher between true
377 negative Ce^* and apparent negative Ce^* (Bau and Dulski, 1996; Planavski et al., 2010),
378 which can arise from the existence of a positive lanthanum anomaly. All our bulk Ce^*
379 represented true negative Ce anomalies (Fig. S4). Samples from MR zone have similar
380 REE+Y patterns compared to older and more recent sediments (from MP1 and MP2 zone,
381 respectively) but slightly differ in terms of Eu^* and Ce^* peak magnitudes and total REE
382 abundance relative to average shale value (Fig. 5, Table 1). This reflects the absence of
383 carbonates in this zone, which otherwise would bring the bulk signature toward a strong
384 negative Ce^* and weak positive Eu^* .

385

386 *4.2.2. Acetic Acid extracts*

387

388 Because calcium carbonate is not present in the samples from MR zone, its chemical variation
389 can only be discussed for MP1 and MP2 zones. REE+Y patterns of samples from MP1 and
390 MP2 zones exhibit a strong negative Ce^* (~ 0.3) and a small positive Eu^* (~ 1.3). We cannot
391 exclude that this latter could result from slight detrital contamination. The Ce^* values are
392 consistent with those of the upper part of the Indian Ocean water column (Byrne and
393 Sholkovitz, 1996) and therefore with a shallow precipitation from phytoplankton. Fe
394 concentrations in the acetic fraction vary between 20 and 50 ppm, and represent a very minor
395 proportion of total Fe (*i.e.* $Fe_{acetic}/Fe_{total} < 0.8\%$, Table S2).

396

397 *4.2.3. Oxalate extracts*

398

399 The oxalate fraction, which is supposed to represent magnetites, contains significant amounts
400 of Al and Mn, with Fe/Al and Mn/Fe molar ratios ranging from 0.33 to 1.95 and 0.02 to 9,
401 respectively. Fe/Al markedly increases at the time of the MECO around 187 mbsf (from 0.8

402 to 2) but then decreases through the rest of MR zone (0.5) and increases above 1 towards the
403 top of the profile (Fig. 4, Table 1). In contrast with bulk data, Fe in the oxalate fraction does
404 not correlate with Al content ($R^2 = 0.15$, figure not shown). Iron concentration varies from
405 0.03 to 0.21 wt % ($Fe_{\text{oxa}}/Fe_{\text{total}}$ between 3 and 14 %, Table S2). Mn/Al shows consistent
406 values in MP1/MP2 zones ($\sim 1.5 \pm 0.3$, $n=8$), a clear decrease at the start of MR zone (0.04)
407 and a slight increase towards its end, with peaks at 184.92 and 184.1 mbsf (6.8 and 3.6,
408 respectively) (Fig. 4, Table 1). Mn concentrations range from 0.04 to 0.11 wt % in MP1/MP2
409 zones and from 0.001 to 0.97 % in MR zone. Ba/Al molar ratio shows a slight increase in MR
410 zone compared to MP1/MP2, from 0.16 to 0.27 on average. Similarly, the sum of REE
411 divided by Al increases from 0.001 to 0.03 on average between MR zone and MP1/MP2
412 zones. Samples from MR zone show true negative Ce^* (0.67 on average). Samples from
413 MP1/MP2 zones show positive and apparent negative Ce^* (due to positive La anomaly) (1.18
414 on average). Positive Eu^* rise up to 58 within MP1/MP2 zones and decrease within MR zone,
415 yet always remaining above 1.50 (Table 1).

416

417 *4.2.4. HF extracts*

418

419 The HF fraction corresponds to the residual phases after acetic acid and oxalate digestion,
420 therefore consisting mostly of detrital silicate components. Fe/Al molar ratio shows a limited
421 range of variation averaging 0.60 ± 0.14 in MP1/MP2 zones and 0.55 ± 0.05 in MR zone (Table
422 1). Fe concentrations vary from 0.4 to 4.4 wt % ($Fe_{\text{HF}}/Fe_{\text{total}}$ between 86 and 96 %, Table S2).
423 Mn/Al ratio averages 0.02 ± 0.01 in MP1/MP2 zones, and 0.01 ± 0.004 in MR zone with notably
424 a clear decrease at 187.02 mbsf. Ba/Al molar ratio increases in MR zone relative to zones
425 MP1 and MP2, from 0.02 to 0.06 on average, with notably a clear increase at 187.02 mbsf.
426 Usual detrital elements like Ti and Zr are well correlated throughout the profile but show a
427 significant increase relative to Al content in MR zone (Table S3).

428 REE/Al ratios mark a clear increase at the start of MR zone that progressively returns to pre-
429 MECO values and end up with a limited increase towards the top. The HF fraction exhibits
430 strong positive Eu^* between ~ 2 and 10, decreasing from 5 to 2.5 at 187.02 mbsf. We find
431 true negative Ce^* within MR zone (0.66 on average), positive Ce^* in MP1 zone and more
432 neutral to negative Ce^* in MP2 zone (0.92 on average).

433

434

435 **4.3. Fe isotope geochemistry**

436

437 Iron isotope compositions were measured on three different fractions (bulk, oxalate and HF
438 fractions) of the sediments throughout the entire profile. Bulk Fe isotope data show very little
439 variations along the stratigraphic profile ($-0.13 \pm 0.04 \text{ ‰}$, $n=24$) and more specifically do not
440 show any variations correlated to the magnetofossils rich layer (MR zone, Fig. 2, Table 2). In
441 contrast, Fe isotope compositions of the oxalate fraction (all duplicated) are roughly constant
442 in MP1 and MP2 zones (with mean $\delta^{56}\text{Fe}$ of $-0.49 \pm 0.04 \text{ ‰}$, $n=8$) but depict a clear
443 stratigraphic trend within the MR zone, decreasing upward from -0.18 to -0.79 ‰ (average -
444 $0.45 \pm 0.23 \text{ ‰}$, $n=9$, Fig. 4, Table 2). Iron extracted by the HF dissolution step shows a
445 limited range of variation of $\delta^{56}\text{Fe}$ value around $-0.08 \pm 0.06 \text{ ‰}$ ($n=17$) and no relation to the
446 stratigraphic layers (Fig. 2, Table 2). The $\delta^{56}\text{Fe}$ values near 0 ‰ observed in bulk and HF
447 fractions are in good agreement with detrital Fe phases from the average continental crust
448 (Beard and Johnson, 2004; Johnson et al., 2008b). In contrast to recent findings in magnetite
449 from magnetotactic bacteria (Amor et al., 2016, 2018), no Fe isotope anomaly was observed
450 in any of the fractions analyzed herein (*i.e.* $\Delta^{57}\text{Fe} \approx 0 \text{ ‰}$).

451

452

453 **5. DISCUSSION**

454

455 **5.1. Efficiency and corrections of the sequential extraction protocol**

456

457 The lack of clear $\delta^{56}\text{Fe}$ trends within the stratigraphic profile of bulk sediments at Hole 711A
458 (Fig. 2), and especially within the MR zone - where magnetofossil abundance increases
459 (Savian et al., 2016) - points out the need for a phase specific analysis of Fe isotopes in order
460 to trace the signature of magnetotactic bacteria (MTB). Sequential extraction procedures have
461 been developed and used in previous studies to examine diverse biogeochemical reaction
462 pathways, Fe-mineral phases and Fe sources (Henkel et al., 2016 and references therein).
463 However, these extraction schemes are not universally applicable and require to consider the
464 specific lithology of each sample (*e.g.* Oonk et al., 2017, Slotznick et al., 2020). Here we have
465 adapted existing protocols to the mineralogy of our samples (see section 3.2). A cautious
466 examination of the chemical composition of different extracts led us to question the efficiency
467 of some of the protocol steps and if it faithfully reflects the isotopic composition of targeted
468 mineral phases. In the following, we discuss the biases of the chemical procedure and how

469 they were corrected before interpreting the data in terms of biosignatures and
470 paleoenvironmental implications.

471

472 *5.1.1. Evidence for multiple mineral phases in the “magnetite extract”*

473

474 The calcium carbonates contained in our samples were efficiently dissolved by reaction with
475 acetic acid (Bayon et al., 2002; Kryc et al., 2003), as demonstrated by comparison between
476 XRD diffractograms (Fig. S1). Perfectly defined calcite peaks were found before (with
477 estimated concentration ~ 95%) *versus* not a single peak after. Acetic acid extracts resulted in
478 Fe concentrations representing less than 0.8% of the total Fe and therefore did not dissolve
479 significant portion of Fe-bearing phases. The most probable iron contamination to the
480 magnetite extract pool would come from the silicate phases, and more specifically clays and
481 zeolites. Previous studies have shown the ability of OA-AO solutions to partially dissolve
482 clay based on pure-phase dissolution tests (from 1 to 10% of its Fe content; Kostka and
483 Luther, 1994; Poulton and Canfield, 2005; supplementary material) or Sr isotope tracing
484 (Winter et al., 1997; Bayon et al., 2002). However zeolite behavior through OA-AO
485 dissolution in conditions similar to those of the present work has never been reported.

486

487 In theory, Fe/Al molar ratios of magnetite and detrital silicate phases are drastically distinct
488 since magnetite (Fe_3O_4) should contain no Al, while detrital silicates such as clays contain
489 more Al than Fe. Fe/Al ratio can thus be used as a proxy of the phases dissolved in the oxalate
490 extractions of our sample. Here, Fe/Al ratios are as low as 0.3 and reach up to 2, overlapping
491 those of the HF fraction (0.4 to 0.9). Such low Fe/Al values can only result from partial
492 dissolution of mineral phases other than magnetite. Although magnetite crystals dominate the
493 magnetic signals of our samples (Savian et al., 2016), they are not the main contributors to
494 bulk iron. Iron is essentially carried by the silicate phase, as demonstrated by (i) the linear
495 correlation between bulk Fe and Al concentrations (Fig. 3), (ii) the similar Fe isotope
496 compositions of bulk and HF fraction and (iii) the recovery rates of Fe between the different
497 fractions (Table S2). Thus, even a low dissolution of silicate phases by the OA-AO attack
498 would result in significant Fe contamination of magnetites. A correlation between Fe and Al
499 concentrations of the oxalate fraction is not observed, which precludes a major contamination
500 by Fe-bearing silicates, without, however, ruling out a subtle dissolution of silicate phases. A
501 few samples are characterized by Fe/Al ratios lower in the oxalate fraction, $(\text{Fe}/\text{Al})_{\text{oxa}}$, than in
502 the HF fraction, $(\text{Fe}/\text{Al})_{\text{HF}}$. This suggests that an Al-rich Fe-poor phase was dissolved during

503 oxalate extraction in addition to the Fe-rich clay. This Al-rich Fe-poor mineral is likely
504 clinoptilolite, a phase observed from our SEM and XRD analyses (see supplementary
505 material) and previously reported in Hole-711A sediments (Hempel and Bohrmann, 1990).
506 Clinoptilolite is an Fe-poor zeolite (Boles, 1972; Mascarenhas et al., 2010; Deer et al., 2013)
507 and if it represents the main contaminant of $(\text{Fe}/\text{Al})_{\text{oxa}}$, it should mostly impact Al content but
508 not $\delta^{56}\text{Fe}_{\text{oxa}}$. We notice a marked difference in $\delta^{56}\text{Fe}$ trends between the oxalate and bulk/HF
509 fractions, suggesting that magnetite has a particular evolution, different from Fe silicate,
510 throughout the stratigraphic profile. However, a contamination might conceal the true $\delta^{56}\text{Fe}$
511 systematic of magnetites, in terms of absolute value and depth profile shape, in particular in
512 samples where the magnetite Fe pool is low with respect to that of total Fe and thus Fe-
513 bearing clay.

514

515 The elemental concentration data of the oxalate fraction also indicate that Mn-oxide was
516 present as well. Indeed, most Mn concentrations of the oxalate fraction were in a similar
517 range or even higher than that of Fe. Unlike Fe, Mn is not enriched in the HF fraction and is
518 unlikely resulting from silicate leaching (average $(\text{Mn}/\text{Al})_{\text{oxa}} \sim 1.36$ vs $(\text{Mn}/\text{Al})_{\text{HF}} \sim 0.01$).
519 Considering either oxic or anoxic conditions, solid Mn-phase other than MnO_2 would not be
520 found at typical seawater alkalinity levels (Calvert and Pederson, 1993). Moreover, no Mn-
521 carbonate was found through XRD. The significance of oxalate-extractable MnO_2 , notably for
522 paleoredox insights, will be discussed later in the paper.

523

524

525 *5.1.2. Assessing Fe isotope composition of Fe-Mn oxides*

526

527 Despite adaptation of existing protocols to our mineralogy, the chemical and isotopic
528 composition of the OA-AO leach clearly consists of a mixture between magnetite and Mn-
529 oxide, and partially dissolved clay and zeolite. Assuming unambiguously depleted, slightly
530 enriched and predominant iron contents for zeolites, clays and Fe-Mn oxides, respectively, the
531 oxalate fraction relates to a 3-endmembers mixing system from which the Fe-Mn oxides
532 isotopic signature can be calculated as a “silicate corrected” signature ($\delta^{56}\text{Fe}_{\text{oxides}}$). Because
533 manganese concentrations in the silicate and metal oxide phases are poorly constrained and/or
534 hardly distinguishable from one another, a correction for Mn-oxides contamination was not
535 possible. Nonetheless, five samples, all within the zone of particular attention for MTB (MR
536 zone; 187.02, 186.92, 185.56, 185.49, 185.31 mbsf) can be extrapolated more closely to pure

537 magnetite since Mn concentrations were negligible in all of them (see supplementary material
538 for details on 185.31 mbsf).

539

540 Numerical corrections using a 3-endmembers mixing approach were applied to determine the
541 true $\delta^{56}\text{Fe}$ values and major/trace elements of Fe-Mn oxides and are presented in details in the
542 supplementary material. The corrected $\delta^{56}\text{Fe}_{\text{oxides}}$ values are reported in Table 2 and their
543 stratigraphic distribution is represented in Figure 4f. Although, they preserve a similar profile,
544 $\delta^{56}\text{Fe}_{\text{oxides}}$ are slightly more negative and span a larger range of values than $\delta^{56}\text{Fe}_{\text{oxa}}$, notably
545 in MR zone (from -0.12 to -0.94 ‰, average -0.48 ± 0.31 ‰, 1SD). In MP1/MP2 zones,
546 $\delta^{56}\text{Fe}_{\text{oxides}}$ show a limited range of variation from -0.48 to -0.61 ‰ (average -0.54 ± 0.05 ‰,
547 1SD).

548

549

550 **5.2. Origin of the iron isotope variations in Fe-Mn oxides**

551

552 *5.2.1. MP1/MP2 Zones*

553

554 Iron isotope compositions in the silicate-corrected oxalate fraction from MP1/MP2 zones can
555 be attributed to biotic / abiotic magnetites and Fe coprecipitated with Mn-oxides (average
556 Mn/Fe = 2.4 ± 0.6 , n=8) in an oxic modern-like ocean. They fall in a very small range of
557 isotopic compositions (Fig. 4f, average $\delta^{56}\text{Fe}_{\text{oxides}} = -0.54 \pm 0.05$ ‰, n=8) while spreading
558 over stratigraphic intervals of several meters (*i.e.* spanning over 2 Ma; Savian et al., 2013).
559 This indicates that they formed through a reproducible process and from a stable Fe source,
560 with limited variation of its Fe isotope composition through time. In modern oxic oceans, the
561 primary sources of Fe are delivered from atmospheric dust particles and hydrothermal fluids
562 (Jickells and Spokes, 2001; Moore and Braucher, 2008; Raiswell and Canfield, 2012). The
563 $\delta^{56}\text{Fe}_{\text{oxides}}$ calculated here cannot be explained by a purely detrital origin as such particles are
564 characterized by a restricted range around 0 ± 0.1 ‰ (Beard and Johnson, 2004), similar to the
565 values found in the residual HF fraction (Fig. 4, Table 1). Alternatively, recycling and
566 fractionation of terrigenous reactive material (close to 0 ‰) through dissimilatory iron
567 reduction (DIR), notably on continental shelves, could constitute a major Fe source to the
568 ocean with negative $\delta^{56}\text{Fe}$ (Elrod et al., 2004; Severmann et al., 2006; Staubwasser et al.,

569 2006). This has been proposed to explain the composition of ferromanganese crusts
570 (Levasseur et al., 2004; Anbar and Rouxel, 2007). Although the contribution of DIR cannot
571 be excluded in the present case, our data are more consistent with a significant hydrothermal
572 contribution. First, our calculated $\delta^{56}\text{Fe}_{\text{oxides}}$ fall in the typical range of hydrothermal fluid and
573 associated fallout sediments that have isotopic compositions between -0.1 and -0.7 ‰,
574 averaging -0.4 ‰ (e.g. Sharma et al., 2001; Severmann et al., 2004; Johnson et al., 2008b;
575 Moeller et al., 2014). Then, a striking positive Eu* anomaly recorded in the oxalate leaches
576 from MP1/MP2 zones (Table 1) is characteristic of hydrothermal fluid, due to Eu(II) leaching
577 from basaltic material interacting with reduced high-T fluids (e.g. German et al., 1990;
578 Klinkhammer et al., 1994). Eu* anomaly and Fe isotope composition thus suggest a strong
579 hydrothermal influence.

580

581 When vent fluids are released in oxic seawaters, hydrothermal $\text{Fe(II)}_{\text{aq}}$ may be quickly and
582 quantitatively oxidized (McDuff, 1995; Field and Sherrell, 2000) such that isotopic
583 compositions of particles in the neutrally buoyant plume and original source $\text{Fe(II)}_{\text{aq}}$ are
584 essentially indistinguishable (Severmann et al., 2004; Moeller et al., 2014). These
585 hydrothermal particles can then be transported and deposited over long distances hundreds of
586 kilometers away (e.g. Chen et al., 1989; Clarkson et al., 2014). Alternatively, if the transfer of
587 Fe from hydrothermal vent to neutrally buoyant plume is not fully conservative (possibly due
588 to faster spreading ridges, more important fluid fluxes or lower $\text{Fe}/\text{H}_2\text{S}, \dots$), Fe loss through
589 rapid Fe-sulfide and/or Fe-oxyhydroxides fallout before all Fe(II) is oxidized may induce
590 fractionation of the buoyant plume (Severmann et al., 2004; Bennett et al., 2009; Rouxel et
591 al., 2008; 2016). In our samples, the strong positive Eu* anomaly and remarkably
592 homogeneous $\delta^{56}\text{Fe}_{\text{oxides}}$ from MP1 and MP2 zones (spanning 2 Ma, in complete oxic
593 conditions, $\text{SD} = 0.05 \text{ ‰}$, $n=8$) suggest that the particles mostly recorded the source
594 composition, with limited secondary Fe isotope fractionation. In addition, Ce* signatures
595 from our oxalate extracts evidence variable interactions of hydrothermal fluids with bottom
596 seawaters. Ce* range from slightly apparent negative to positive anomalies (Fig. 5). Oxic
597 waters usually display negative Ce* because Ce(IV) forms oxide particles and/or is
598 preferentially adsorbed on Fe/Mn-oxyhydroxides, organic matter and clay surfaces (German
599 and Elderfield, 1990; Byrne and Sholkovitz, 1996; Haley et al., 2004) compared to other
600 REE(III). Particles forming in a hydrothermal plume will scavenge REE from both seawater
601 and hydrothermal fluids, acquiring more or less the respective negative Ce* and positive Eu*
602 anomalies depending on the degree of mixing (German et al., 1990; Byrne and Sholkovitz.,

603 1996; Chavagnac et al., 2005; Mascarenhas et al., 2010), a process supported by the
604 correlation between Eu* and Ce* from MP1/MP2 zones (Fig. S5).

605

606 In summary, Fe-Mn oxides from MP1/MP2 zones are dominated by particles from more or
607 less diluted hydrothermal plumes, that interacted with oxic seawater for varying amounts of
608 time. If Fe/Mn-oxides in this zone do not inform us about magnetofossil geochemical
609 signatures, they provide a good constrain on the hydrothermal contribution to Hole 711A,
610 which likely did not stop through MR zone and the MECO.

611

612

613 *5.2.2. MR Zone*

614

615 The $\delta^{56}\text{Fe}_{\text{oxides}}$ profile from MR zone is markedly different from that of the two other sections,
616 located above and below, and perfectly matches the interval described as magnetofossils-rich
617 based on magnetic data (Fig. 4f; Savian et al., 2016). The $\delta^{56}\text{Fe}_{\text{oxides}}$ values show a significant
618 decrease upwards, from -0.12 to -0.94 ‰. While the hydrothermal influence is still present, an
619 additional source of Fe seems to contribute to the samples from MR zone, recording the
620 MECO event. We discuss below the Fe source changes as well as diagenetic processes
621 inducing Fe isotope variability in the oxide fraction of MR zone.

622

623 *5.2.2.1. New iron supply*

624

625 As a result of rising global temperatures during hyperthermal events like the MECO, it has
626 been proposed that surface waters nutrients and/or Fe fertilization increased due to (1) aeolian
627 dust from drier regions (Roberts et al., 2011; Savian et al., 2014, 2016), (2) continental
628 weathering and runoff from wetter regions (Spofforth et al., 2010; Luciani et al., 2010;
629 Moebius et al., 2014) and/or (3) a change in ocean circulation (Witkowski et al., 2012;
630 Moebius et al., 2014). Since the paleodepositionnal site of Hole 711A was located in pelagic
631 domain of the open ocean, a large Fe contribution from continental runoff is unlikely. The
632 present data rather support a scenario involving a new source of reactive Fe added to
633 hydrothermal particles at the time of the MECO (samples 187.02 and 186.91 mbsf), and could
634 correspond to enhanced atmospheric fallout.

635

636 Firstly, although Eu* anomalies in the oxalate fraction of MR zone are still well above 1, they

637 are on average 8 times smaller than in MP1/MP2 zones and thus indicate that hydrothermal
638 influence was diminished or diluted by another component. Concomitantly, a marked increase
639 of Fe concentrations from 0.03 to 0.21 wt % is observed at 187.02 mbsf, indicating that a new
640 source of Fe was added to hydrothermal input already present in MP1 zone. Furthermore, Fe-
641 Mn oxides from MR zone recorded higher REE contents (as REE/Al) in comparison to
642 hydrothermally dominated MP1/MP2 samples. This suggests that REE-enriched particles
643 were delivered to Hole 711A sediments during the MECO event. They could have been
644 Mn/Fe-oxyhydroxides, which are efficient in scavenging REE, while descending through the
645 water column (German et al., 1990; Byrne and Sholkovitz, 1996; Ohta and Kawabe, 2001;
646 Planavsky et al., 2010). In the HF fraction, usual detrital elements like Ti and Zr normalized
647 by Al slightly increase within MR zone, also suggesting a different supply of detrital
648 components. Fe isotopic composition of the source determined for MR zone from diagenetic
649 modeling is consistent with this change in Fe supply (see section 5.2.2.2 below). Thus,
650 sediments from Hole 711A record an additional supply of Fe consequently to the MECO,
651 which probably influenced MTB activity and magnetofossils isotopic compositions.

652

653

654 *5.2.2.2. Diagenetic processes and isotopic variability*

655

656 In addition to Fe source changes, redox perturbations induced isotopic variability within the
657 authigenic oxide fraction of MR zone. The first samples deposited in this stratigraphic interval
658 (187.02, 186.91, 185.56, 185.49 mbsf) have Mn/Fe ratios between 0.01 and 0.02 and are thus
659 devoid of Mn-oxides. This leaves magnetite – most likely as magnetofossils (Savian et al.,
660 2016) - as the main mineral phase of the Fe-Mn oxide fraction at these depths. Upwards in
661 MR zone, the general decrease of $\delta^{56}\text{Fe}_{\text{oxides}}$ down to -0.94‰ cannot be inherited from a
662 mixing of magnetofossils with a component enriched in Mn and light Fe isotopes since typical
663 mixing diagram such as $\delta^{56}\text{Fe}_{\text{oxides}}$ vs Mn/Fe ratio should display a linear correlation, which is
664 not observed. In contrast, a plot of $\delta^{56}\text{Fe}_{\text{oxides}}$ vs Mn/Fe ratio (as well as $\delta^{56}\text{Fe}_{\text{oxides}}$ versus other
665 typical hydrothermal metalloids Ni, Mo, V, Cu, Co, Ti and Zn normalized by Fe) exhibits
666 well-defined logarithmic variation ($R^2=0.95$ for Mn/Fe, Fig. 6). Only one sample (185.31
667 mbsf) is outside of the correlation but is likely affected by post-depositional and/or side
668 effects and was most likely devoid of Mn oxides at time of deposition (see supplementary
669 material).

670

671 Overall, the iron isotope composition of the Fe-Mn oxides fraction becomes lighter as the iron
672 content decreases relative to these elements. The trend is compatible with a Rayleigh
673 distillation process, where Fe in magnetite or associated to Mn oxides is progressively
674 precipitated from a limited dissolved Fe reservoir. We modeled the concomitant decrease of
675 $\delta^{56}\text{Fe}_{\text{oxides}}$ and iron content relative to the aforementioned elements using Rayleigh equations
676 as,

$$677 \quad \delta_{\text{fluid}} = \delta_0 + 1000 \times (\alpha - 1) \times \ln F \quad (3)$$

$$678 \quad \text{and } \Delta_{\text{fluid-oxide}} = \delta_{\text{fluid}} - \delta_{\text{oxide}} \approx 1000 \ln \alpha \quad (4)$$

679 where δ_0 and δ_{fluid} are the initial and residual Fe isotope compositions of the fluid, F is the Fe
680 fraction remaining in the fluid (calculated relative to metals like Mn), α is the fractionation
681 factor between fluid and oxides, $\Delta_{\text{fluid-oxide}}$ is the Fe isotope fractionation between fluid and
682 oxide, and δ_{oxide} is the isotope composition of the oxide precipitate. The best fit to our data is
683 found for initial fluid composition of -0.36 ‰ and Fe isotope fractionation of +0.09 ‰
684 between fluid and precipitate (Fig. 6). Interestingly, the initial fluid composition determined
685 by our model is higher than that estimated for hydrothermal sources at Hole 711A through
686 MP1/MP2 zones (avg -0.54 ‰). This may reflect the input of an additional, heavy iron source
687 during the MECO, which is consistent with the delivery of aeolian particulate Fe (with $\delta^{56}\text{Fe}$
688 near 0 ‰; Beard et al., 2003; Johnson et al., 2020) to the ocean at that time (Savian et al.,
689 2014; 2016). Iron isotope modeling thus supports the hypothesis of an additional atmospheric
690 Fe supply during the MECO event.

691

692 The global stratigraphic trend of Fe-Mn oxides in MR zone implies that conditions evolved
693 from an Fe-rich to Fe-limited reservoir, relative to Mn enrichment upward. This can be
694 explained by a shift from anoxic conditions in the lower part of MR zone to suboxic
695 conditions in the upper part, until fully oxic conditions returned in MP2 zone. In detail,
696 sediments from MR zone probably experienced vertical fluctuations of a redox front. This is
697 well illustrated by Mn content variations along the stratigraphic profile (Table 1). High Mn
698 concentrations of the sediments represent times of oxic to nitrogenous conditions while low
699 Mn concentrations in sediments would have arisen under manganoous or ferruginous
700 conditions (Canfield and Thamdrup, 2009; Roberts, 2015). The dramatic decrease of Mn
701 content at the start of MR zone, and increase higher than any other sample at 184.92 mbsf
702 indicates that Fe-Mn oxyhydroxide particles dissolved under reducing conditions (Roberts,
703 2015), such that Mn^{2+} accumulated in sediment porewater, possibly up to the water-sediment

704 interface, and later precipitated as Mn-oxides when more oxidizing conditions were reached
705 again (Klinkhammer and Bender, 1980; Burdige and Gieskes, 1983; Chun et al., 2010). In the
706 reducing conditions prevailing at the start of MR zone, most reactive Fe minerals (*e.g.*
707 ferrihydrite, lepidocrocite; Canfield et al., 1992) whose supply was likely enhanced at this
708 time (*see section 5.2.2.1*), would have dissolved and provided an Fe source for MTB.

709

710 In summary, iron isotope and trace element compositions show that the oceanic Fe
711 biogeochemical cycle was strongly modified during the MECO, from surface to bottom layers
712 even at a pelagic site, and not only in near-shore environments as previously established
713 (Savian et al., 2014). Moreover, this led to important redox perturbations within the sediment
714 column and/or near water-sediment interface.

715

716

717 **5.3. Iron isotope signature of magnetofossils**

718

719 Iron isotope fractionations linked to MTB activity have been examined in a limited number of
720 previous studies, based on laboratory cultures only (Mandernack et al., 1999; Amor et al.,
721 2016; 2018). The present contribution represents the first attempt to characterize MTB
722 biogeochemical signature in the sedimentary record. As discussed above (section 5.2.2.2), the
723 $\delta^{56}\text{Fe}_{\text{oxides}}$ vs Mn/Fe trend observed in MR zone sediments can be attributed to a Rayleigh
724 distillation process related to Fe precipitation as biomagnetite and/or Fe-Mn oxide. However,
725 the five samples located in the lower part of MR zone are devoid of Mn-oxide and thus
726 represent a pure magnetite endmember. Though a small portion of it could derive from
727 increased detrital inputs, most of them fall at the peak abundance of magnetofossils (Savian et
728 al., 2016). These findings support that $\delta^{56}\text{Fe}_{\text{oxides}}$ values of these specific samples can be
729 ascribed to magnetofossils. They vary from -0.12 to -0.34 ‰ (Table 2). It can be noted that if
730 10% of the magnetite fraction would be detrital with $\delta^{56}\text{Fe}$ of 0 ± 0.1 ‰ (Beard and Johnson,
731 2004), this would not change the magnetofossil $\delta^{56}\text{Fe}$ values by more than 0.04 ‰, which is
732 negligible. It is thus reasonable to consider these values as representative of magnetofossils.
733 Assuming the isotope composition of the initial Fe-rich fluid was -0.36 ‰, as deduced from
734 our Rayleigh model for MR zone (Fig. 6), the Fe isotope fractionation between the modeled
735 fluid and the purported magnetofossils is comprised between 0.06 and 0.30 ‰, with an
736 average of 0.19 ± 0.10 ‰. This fractionation is similar, within uncertainty, to the value

737 determined above from the Rayleigh model even for samples enriched in Mn (0.1‰; Fig. 6).
738 This implies that Fe depletion relative to Mn may be due to Fe sequestration in magnetite of
739 magnetotactic bacteria rather than adsorption or co-precipitation to Mn oxides, even though it
740 cannot be firmly demonstrated.

741

742 The Fe isotope fractionation between fluid and biogenic magnetite determined here (0.1 to
743 0.3‰) is very low and similar to the one predicted from MTB laboratory cultures by
744 Mandernack et al. (1999) (Fig. 7), who concluded to negligible fractionation. In the present
745 samples, the MTB strains that precipitated magnetofossils remain unknown but could possibly
746 impact the Fe isotope composition through different metabolic pathways. The work by
747 Mandernack et al. (1999) was conducted on two different MTB strains, MS-1 and MV-1,
748 cultivated under variable conditions. The strain MS-1 is a freshwater bacterium and was
749 cultivated under microaerophilic conditions while MV-1 is a marine bacterium and was
750 grown anaerobically (Mandernack et al., 1999). No significant difference was found between
751 the two distinct strains in this pioneer study. In contrast, later experimental work reported
752 strong Fe isotope fractionation for the freshwater strain AMB-1, with biogenic magnetite
753 depleted in heavy isotope by 2‰ relative to the growth media (Amor et al., 2016, 2018). The
754 work on AMB-1 also highlighted a unique mass independent signature in biogenic magnetite
755 (Amor et al., 2016, 2018), where the odd isotope (^{57}Fe) was incorporated preferentially
756 relative to even isotopes (^{54}Fe , ^{56}Fe , ^{58}Fe). In the present study, the results of the five samples
757 from the lower part of MR zone are strikingly different from those obtained on AMB-1 since
758 we observed slight enrichment in heavy isotope (rather than strong depletion, Fig. 7) and no
759 isotope anomaly on ^{57}Fe . The origin of the discrepancy between the two laboratory cultures
760 on strains AMB-1 (Amor et al., 2016, 2018) and MV1 and MS-1 (Mandernack et al., 1999) is
761 not clear (see discussion in Amor et al., 2018) and it is thus difficult to extrapolate them to our
762 natural environment. It may have arisen from various biological pathways and/or specific
763 growth conditions such as Fe concentration. It is noteworthy that the overall MTB cells were
764 found to be positively fractionated relative to the growth media due to storing of heavy Fe
765 isotopes in the bacterial lysate (membrane, cytoplasm and periplasm) even though
766 magnetosomes were isotopically light (Amor et al., 2016, 2018). A complete transfer of Fe
767 from the inner cell reservoirs to magnetosome magnetite would thus impart a slight positive
768 Fe isotope signature to the magnetite crystals. Finally, the diagenetic processes related to
769 sediment burial may lead to Fe isotopes exchange between the cells and magnetosomes and
770 will need to be addressed in the context of natural ancient samples.

771

772 Finally, iron isotope fractionation calculated here between fluids and magnetofossil (+0.1 to
773 +0.3‰) is low compared with the value determined experimentally between abiotic magnetite
774 and dissolved Fe(II) ($\Delta^{56}\text{Fe}_{\text{mag-Fe(II)}} = 1.5 \text{ ‰}$, Fig. 7; Johnson et al., 2005; Frierdich et al.,
775 2014). This implies that Fe isotope may be used as a tracer of biological magnetite formed by
776 MTB even for limited fractionation. More work based on laboratory cultures and natural
777 environment is still required to confirm this result and better define this potential proxy.

778

779

780 **5.4. Magnetofossil preservation in sedimentary rocks**

781

782 Another important result inferred from the present data concerns magnetofossils preservation.
783 XRD and SEM analyses confirmed the presence of barite (barium sulfate) throughout the
784 stratigraphic section in Hole 711A, and in particular during the MECO event (Hempel and
785 Bohrmann, 1990). The presence of sulfates as a solid phase might be a key criterion for
786 magnetofossils preservation. Indeed, magnetites produced by MTB are poorly preserved in
787 sediments because they are actively dissolved when aqueous sulfides are produced in
788 porewaters (Canfield and Berner, 1987; Karlin et al., 1990a; 1990b; Yamazaki et al., 2003;
789 Kopp and Kirschvink, 2008; Roberts, 2015). If high organic matter flux is exported to a
790 sediment, dissimilatory iron reduction (DIR), that generates ferruginous conditions in which
791 MTB thrive, is followed by bacterial sulfate reduction (BSR) that uses dissolved sulfate as the
792 next electron acceptor (Froelich et al., 1979; Hesse, 1994; Canfield and Thamdrup, 2009). As
793 a result, many environments in which MTB have flourished do not preserve their magnetic
794 signature because magnetosomes are ultimately dissolved by BSR-produced sulfides (*e.g.*
795 Canfield and Berner, 1987; Emiroglu et al., 2004; Mohamed et al., 2011). At Hole 711A,
796 important quantities of Ba (up to $\sim 1.3 \text{ wt } \%$) were recovered at depths with abundant
797 magnetofossils (MR zone). They are likely due to important barite concentrations derived
798 from increased primary productivity export and hydrothermal contribution (see *section 5.5*).
799 In this environment, the precipitation of barite may have sufficiently decreased the SO_4^{2-}
800 concentration in porewaters to prevent abundant sulfide formation by BSR activity and
801 subsequent magnetite dissolution. Alternatively, all the organic matter in the sediments may
802 have been degraded before complete anoxia and before BSR could significantly proceed. In
803 contrast to manganese, the absence of barium concentration drop followed by an enriched
804 layer in the bulk or in any of the sequentially extracted fractions of the studied interval,

805 suggests that sulfate reduction and subsequent re-oxidation did not occur or only to a minor
806 extent (Dymond et al., 1992; Tribovillard et al., 2006). Magnetic and microscopic (TEM)
807 identification of magnetofossils in Hole 711A samples (Chang et al., 2012; Savian et al.,
808 2016) also show that magnetofossils did not undergo reductive dissolution. In other words,
809 the ferruginous – sulfidic transition characteristic of diagenetic processes did not happen, or
810 with only limited sulfides production (also supported by the absence of pyrite in XRD and
811 SEM analyses; Canfield and Thamdrup, 2009; Roberts, 2015). Hence, optimal environmental
812 conditions were met for MTB to thrive at the time of MR zone sediments deposition and be
813 subsequently preserved (Roberts et al., 2011; Roberts, 2015; Savian et al., 2016).

814

815

816 **5.5. Paleoenvironmental implications for the MECO**

817

818 The MECO event has been documented in several Deep Sea Drilling Project (DSDP) and
819 ODP sites - including Hole 711A – and represent a global warming event, affecting many
820 biogeochemical parameters of the atmosphere-ocean system (*e.g.* Bohaty and Zachos, 2003;
821 Bohaty et al., 2009; Bijl et al. 2010; Spofforth et al. 2010; Savian et al. 2014, 2016; Edgar et
822 al., 2020). One of the most visible effect of the MECO at Hole 711A is the shallowing of
823 calcite compensation depth (CCD), leading to calcite dissolution in the water column and
824 water-sediment interface (Bohaty et al., 2009). As discussed above, our geochemical data
825 foster the idea that iron supply to the ocean by aeolian dust fallout was enhanced during the
826 MECO event. Because Fe is a limiting nutrient to microorganisms, Fe fertilization should
827 have led to eutrophication of the ocean and increased primary productivity (Martin et al.,
828 1991; Jickells et al., 2005; Boyd and Ellwood, 2010). Previous studies of calcareous and
829 siliceous microfossil assemblages in worldwide sediments have highlighted such a shift in
830 trophic state during the MECO (Moebius et al, 2014, 2015; Villa et al., 2014; Witkosky et al.,
831 2012, 2014; Luciani et al., 2010, Toffanin et al., 2011). A similar study is still lacking for the
832 Indian Ocean though existing for the Southern Ocean. However, barium abundances
833 measured herein can be used as a paleoproductivity proxy (Dymond et al., 1992; McManus et
834 al., 1999; Tribovillard et al., 2004; Riquier et al., 2005; Paytan and Griffith, 2007;
835 Bridgestock et al., 2019), and further support an increase of organic matter (OM) export as a
836 response to the MECO near Hole 711A (Savian et al., 2016).

837 Indeed, barite tends to precipitate in supersaturated micro-environments forming from organic

838 matter degradation, in oceans that are otherwise undersaturated with respect to this mineral
839 (Dehairs et al., 1980; Dymond et al., 1992; Paytan and Griffith, 2007). As long as sulfate-
840 reduction did not occur, increased Ba concentrations are normally indicative of increased
841 organic matter burial (Tribovillard et al., 2006). The use of Ba/Al ratio in specific leaches
842 rather than Ba concentration allows us to avoid any dilution artifacts (which were also
843 accounted for following the approach of Torfstein et al. (2010), using age model from Savian
844 et al. (2013), see supplementary material, Table S4).

845 Both the oxalate and HF fractions present increased Ba/Al ratios within MR zone. Barium
846 contributions from detrital inputs are considered negligible in pelagic environments (Dymond
847 et al., 1992; Reitz et al., 2004) and were estimated to only represent a few percent of the total
848 Ba content in our samples (even using highest Ba/Al_{detrital} estimates; Reitz et al., 2004). Thus,
849 high Ba concentrations reported here (up to ~ 1.3 wt % in MR zone) can only be
850 accommodated by the presence of a Ba-rich phase like barite (BaSO₄), of hydrothermal and/or
851 biogenic origin (Bridgestock et al., 2019). As discussed above in section 5.4, redox re-
852 mobilization/precipitation of barite would have been negligible in our samples. Hydrothermal
853 input may account for a part of the Ba content measured at Hole 711A since hydrothermal
854 contribution is evidenced from positive Eu* anomaly. However, it usually represents minor
855 input even in hydrothermally-dominated Mn/Fe-oxides of sediments located close to venting
856 sites (Dymond et al., 1992; Paytan and Griffith, 2007). Besides, the sharp Ba/Al increase in
857 the HF fraction at the MECO (*i.e.* ~ 187 mbsf) corresponds to a net decrease in Eu*,
858 suggesting that Ba increase does not primarily reflect hydrothermalism. Similarly, Ba/Al
859 ratios of the oxalate fraction increase through MR zone while Eu* anomalies are markedly
860 lower in this zone. Therefore, elevated Ba/Al ratios in our samples from the MECO event
861 most likely reflect increased export productivity and barite precipitation due to OM decay in
862 the water column and sediments.

863 Enhancement of primary productivity through iron fertilization creates ideal conditions for
864 MTB growth and expansion in sediments because it provides a source of both Fe and OM,
865 and generates suboxic zones from OM decay (Roberts et al., 2011; Chang et al., 2012; Villa et
866 al., 2014). A decrease of dissolved oxygen level in the ocean is also favored by increased gas
867 exchange in warmer and higher atmospheric CO₂ condition characteristic of hyperthermal
868 events (Chun et al., 2010). The relations between Fe isotope composition and Mn content
869 observed in our dataset show that important redox changes occurred in the open Indian Ocean
870 in response to the MECO event. Together with the lower redox limit fixed by the continuous

871 presence of barite, the various geochemical proxies presented here thus show that ideal
872 environmental conditions close to the manganous-ferruginous zone were met for MTB to
873 thrive in MR zone.

874

875 **6. CONCLUSIONS AND SUMMARY**

876

877 Our study represents the first attempt to characterize the geochemical biosignature of MTB in
878 the sedimentary record. We combine Fe isotopes with major and trace elements to describe
879 magnetofossils in relation with the complex environmental changes of the MECO and we
880 shed light on analytical and theoretical difficulties that can arise from ancient natural samples
881 compared to laboratory investigations.

882 Because Fe is a major constituent of numerous mineralogical phases, bulk Fe isotope
883 measurements from sedimentary rocks are unlikely to mirror solely that of magnetite (Figs. 2e
884 and 4f), even though the latter might dominate the magnetic signal. A selective extraction of
885 magnetite is required for magnetofossils interpretation. Here we show that magnetite isotopic
886 composition can be more or less contaminated through chemical extraction depending on the
887 mineralogy of the treated samples. Therefore, a great attention must be paid to sample
888 lithology before application of a sequential extraction procedure in order to (i) optimize the
889 extraction protocol, (ii) apply possible numerical corrections and (iii) critically interpret the
890 results. In the future, magnetic extraction followed by isotopic measurements will have to be
891 tested as an alternative to chemical extraction. The main challenge will be to obtain
892 chemically pure fraction in sufficient amount for geochemical analyses. The small grain size
893 (*i.e.* submicrometer) may limit our ability to separate and purify magnetically the magnetite
894 fraction.

895 In sediments from ODP Hole 711A, complementary analyses of the other Fe-bearing phases
896 allowed us for correction and interpretation of the true magnetite $\delta^{56}\text{Fe}$ values in the
897 magnetofossil-rich stratigraphic interval, specifically in the lower part of MR zone where no
898 Fe-Mn oxides were present. Although magnetofossils from MR zone did not record highly
899 negative and/or mass-independent fractionation as expected from some laboratory studies
900 (Amor et al., 2016; 2018), the slightly positive fractionation ($\sim 0.1\text{-}0.3\text{‰}$) is distinguishable
901 from that of abiotic magnetite (Johnson et al., 2005; Frierdich et al., 2014) and can therefore

902 be used as a biosignature for MTB in past environments. More work on natural and laboratory
903 samples is needed to assess the dependence of this fractionation on parameters such as MTB
904 strain, concentration of bioavailable Fe, conditions of preservation of the cell and
905 magnetosomes through time.

906 Importantly, our results suggest that the presence of sulfate minerals could be a prerequisite
907 for magnetofossils preservation in environments where dissolved sulfates are present, as the
908 capture of sulfate could reduce the production of sulfides in suboxic/anoxic settings and thus
909 the dissolution of magnetite.

910 Finally, several geochemical proxies are used to describe the paleoenvironmental changes
911 occurring during the MECO and recorded at deep pelagic site ODP Hole 711A. Specifically,
912 increased Fe supply to the surface Indian Ocean most likely affected the biogeochemical
913 cycle of this element down to pelagic settings and increased primary productivity of the
914 ocean, which may have supported the recovery from the MECO warming. Higher OM export
915 to the sediments explain the shift to lower redox potential conditions observed in MR zone
916 and increased Ba concentrations. Thereby, this influenced mineral dissolution (*e.g.* Mn-
917 oxides, reactive Fe-oxyhydroxides) and precipitation (*e.g.* magnetite) in the sediment and
918 allowed MTB to flourish and be subsequently preserved, as a consequence of the MECO.

919

920 **Acknowledgments**

921

922 Ricardo Trindade, Luigi Jovane, François Mathon, Matthieu Amor, Eric Siciliano Rego and
923 colleagues from the stable isotope laboratory are thanked for help and discussions.
924 Collaboration with Christopher Lefèvre strongly motivated this study. R.H. and V.B. were
925 supported by the French National Research Agency (SIGMAG: ANR-18-CE31-0003) and the
926 Institut de Physique du Globe de Paris. V.B. thanks the Institut Universitaire de France for
927 funding (IUF#2017-2021). R.H. and V. B. would like to thank Pascale Louvat, Pierre
928 Burckel, Sophie Nowak, Stefan Borensztajn and Christophe Thomazo for their analytical
929 assistance and discussions. We also acknowledge the Integrated Ocean Drilling Program
930 (IODP) for providing the samples used in this research. JFS thanks the National Council for
931 Scientific and Technological Development (CNPq, Brazil) grants #201508/2009- 5; #427280/
932 2018-4 and Fundação de Amparo à Pesquisa do Estado do Rio Grande do Sul (FAPERGS,

933 Brazil) grant #16/2551-0000213-4.

934

935 **References**

- 936 Amor, M., Busigny, V., Louvat, P., Gélabert, A., Cartigny, P., Durand-Dubief, M., Ona-
937 Nguema, G., Alphandéry, E., Chebbbi, I. and Guyot, F. (2016). Mass-dependent and -
938 independent signature of Fe isotopes in magnetotactic bacteria. *Science*, 352(6286),
939 705–708.
- 940 Amor, M., Busigny, V., Louvat, P., Tharaud, M., Gélabert, A., Cartigny, P., Carlut, J.,
941 Isambert, A., Durand-Dubief, M., Ona-Nguema, G., Alphandéry, E., Chebbbi, I. and
942 Guyot, F. (2018). Iron uptake and magnetite biomineralization in the magnetotactic
943 bacterium *Magnetospirillum magneticum* strain AMB-1: An iron isotope study.
944 *Geochimica et Cosmochimica Acta*, 232, 225–243.
- 945 Amor, M., Mathon, F. P., Monteil, C. L., Busigny, V., and Lefevre, C. T. (2020). Iron-
946 biomineralizing organelle in magnetotactic bacteria: function, synthesis and
947 preservation in ancient rock samples. *Environmental Microbiology*, 22(9), 3611-3632.
- 948 Anbar, A. D., and Rouxel, O. (2007). Metal Stable Isotopes in Paleoceanography. *Annual*
949 *Review of Earth and Planetary Sciences*, 35(1), 717–746.
- 950 Archer, C., and Vance, D. (2006). Coupled Fe and S isotope evidence for Archean microbial
951 Fe(III) and sulfate reduction. *Geology*, 34(3), 153.
- 952 Backman, J., Duncan, R. A., and et al. (Eds.). (1988). *Proceedings of the Ocean Drilling*
953 *Program, 115 Initial Reports* (Vol. 115). Ocean Drilling Program.
- 954 Bau, M., and Dulski, P. (1996). Distribution of yttrium and rare-earth elements in the Penge
955 and Kuruman iron-formations, Transvaal Supergroup, South Africa. *Precambrian*
956 *Research*, 79(1), 37–55.
- 957 Bayon, G., German, C. R., Boella, R. M., Milton, J. A., Taylor, R. N., and Nesbitt, R. W.
958 (2002). An improved method for extracting marine sediment fractions and its
959 application to Sr and Nd isotopic analysis. *Chemical Geology*, 187(3–4), 179–199.
- 960 Bazylinski, D. A., and Frankel, R. B. (2003). Biologically Controlled Mineralization in
961 Prokaryotes. *Reviews in Mineralogy and Geochemistry*, 54(1), 217–247.
- 962 Beard, B. L., and Johnson, C. M. (2004). Fe Isotope Variations in the Modern and Ancient
963 Earth and Other Planetary Bodies. *Reviews in Mineralogy and Geochemistry*, 55(1),
964 319–357.
- 965 Beard, B. L., Johnson, C. M., Von Damm, K. L., and Poulson, R. L. (2003). Iron isotope
966 constraints on Fe cycling and mass balance in oxygenated Earth oceans. *Geology*,
967 31(7), 629–632.
- 968 Belshaw, N. S., Zhu, X. K., Guo, Y., and O’Nions, R. K. (2000). High precision measurement
969 of iron isotopes by plasma source mass spectrometry. *International Journal of Mass*
970 *Spectrometry*, 197(1–3), 191–195.
- 971 Bennett, S. A., Rouxel, O., Schmidt, K., Garbe-Schönberg, D., Statham, P. J., and German, C.
972 R. (2009). Iron isotope fractionation in a buoyant hydrothermal plume, 5°S Mid-
973 Atlantic Ridge. *Geochimica et Cosmochimica Acta*, 73(19), 5619–5634.

- 974 Bijl, P. K., Houben, A. J. P., Schouten, S., Bohaty, S. M., Sluijs, A., Reichart, G.-J.,
975 Sinninghe Damsté, J. and Brinkhuis, H. (2010). Transient Middle Eocene
976 Atmospheric CO₂ and Temperature Variations. *Science*, 330(6005), 819–821.
- 977 Bohaty, S. M., and Zachos, J. C. (2003). Significant Southern Ocean warming event in the
978 late middle Eocene. *Geology*, 31(11), 1017–1020.
- 979 Bohaty, S. M., Zachos, J. C., Florindo, F., and Delaney, M. L. (2009). Coupled greenhouse
980 warming and deep-sea acidification in the middle Eocene. *Paleoceanography*,
981 24(PA2207).
- 982 Boles, J. R. (1972). Composition, optical properties, cell dimensions, and thermal stability of
983 some heulandite group zeolites. *American Mineralogist: Journal of Earth and
984 Planetary Materials*, 57(9–10), 1463–1493.
- 985 Boscolo Galazzo, F., Thomas, E., and Giusberti, L. (2015). Benthic foraminiferal response to
986 the Middle Eocene Climatic Optimum (MECO) in the South-Eastern Atlantic (ODP
987 Site 1263). *Palaeogeography, Palaeoclimatology, Palaeoecology*, 417, 432–444.
- 988 Boyd, P. W., and Ellwood, M. J. (2010). The biogeochemical cycle of iron in the ocean.
989 *Nature Geoscience*, 3(10), 675–682.
- 990 Bridgestock, L., Hsieh, Y.-T., Porcelli, D., and Henderson, G. M. (2019). Increased export
991 production during recovery from the Paleocene–Eocene thermal maximum
992 constrained by sedimentary Ba isotopes. *Earth and Planetary Science Letters*, 510,
993 53–63.
- 994 Burdige, D. J., and Gieskes, J. M. (1983). A pore water/solid phase diagenetic model for
995 manganese in marine sediments. *American Journal of Science*, 283(1), 29–47.
- 996 Byrne, R. H., and Sholkovitz, E. R. (1996). Marine chemistry and geochemistry of the
997 lanthanides. *Handbook on the Physics and Chemistry of Rare Earths*, 23, 497–593.
- 998 Calvert, S. E., and Pedersen, T. F. (1993). Geochemistry of Recent oxic and anoxic marine
999 sediments: Implications for the geological record. *Marine Geology*, 113(1–2), 67–88.
- 1000 Canfield, D.E., Raiswell, R., Bottrell, S.H., 1992. The reactivity of sedimentary iron minerals
1001 toward sulfide. *Am. J. Sci.* 292, 659–683.
- 1002 Canfield, D. E., and Berner, R. A. (1987). Dissolution and pyritization of magnetite in anoxic
1003 marine sediments. *Geochimica et Cosmochimica Acta*, 51(3), 645–659.
- 1004 Canfield, D. E., and Thamdrup, B. (2009). Towards a consistent classification scheme for
1005 geochemical environments, or, why we wish the term ‘suboxic’ would go away.
1006 *Geobiology*, 7(4), 385–392.
- 1007 Chang, L., Roberts, A. P., Williams, W., Fitz Gerald, J. D., Larrasoana, J. C., Jovane, L., and
1008 Muxworthy, A. R. (2012). Giant magnetofossils and hyperthermal events. *Earth and
1009 Planetary Science Letters*, 351–352, 258–269.
- 1010 Chang, S. B. R., and Kirschvink, J. L. (1989). Magnetofossils, the Magnetization of
1011 Sediments, and the Evolution of Magnetite Biomineralization. *Ann. Rev. Earth Planet.
1012 Sci*, 17, 169–195.
- 1013 Chavagnac, V., German, C. R., Milton, J. A., and Palmer, M. R. (2005). Sources of REE in
1014 sediment cores from the Rainbow vent site (36°14'N, MAR). *Chemical Geology*,
1015 216(3), 329–352.

- 1016 Chen, J. C., and Owen, R. M. (1989). The hydrothermal component in ferromanganese
1017 nodules from the southeast Pacific Ocean. *Geochimica et Cosmochimica Acta*, 53(6),
1018 1299–1305.
- 1019 Chun, C. O. J., Delaney, M. L., and Zachos, J. C. (2010). Paleoredox changes across the
1020 Paleocene-Eocene thermal maximum, Walvis Ridge (ODP Sites 1262, 1263, and
1021 1266): Evidence from Mn and U enrichment factors. *Paleoceanography*, 25(4).
- 1022 Clarkson, M. O., Poulton, S. W., Guilbaud, R., and Wood, R. A. (2014). Assessing the utility
1023 of Fe/Al and Fe-speciation to record water column redox conditions in carbonate-rich
1024 sediments. *Chemical Geology*, 382, 111–122.
- 1025 Dauphas, N., Janney, P. E., Mendybaev, R. A., Wadhwa, M., Richter, F. M., Davis, A. M.,
1026 van Zuilen, M., Hines, R. and Foley., C. N. (2004). Chromatographic Separation and
1027 Multicollection-ICPMS Analysis of Iron. Investigating Mass-Dependent and -
1028 Independent Isotope Effects. *Analytical Chemistry*, 76(19), 5855–5863.
- 1029 Dauphas, N., Pourmand, A., and Teng, F.-Z. (2009). Routine isotopic analysis of iron by HR-
1030 MC-ICPMS: How precise and how accurate? *Chemical Geology*, 267(3–4), 175–184.
- 1031 Deer, W. A., Howie, R. A., and Zussman, J. (2013). *An Introduction to the Rock-Forming*
1032 *Minerals*. Mineralogical Society of Great Britain and Ireland.
- 1033 Dehairs, F., Chesselet, R., and Jedwab, J. (1980). Discrete suspended particles of barite and
1034 the barium cycle in the open ocean. *Earth and Planetary Science Letters*, 49(2), 528–
1035 550.
- 1036 Dinarès-Turell, J., Hoogakker, B.A., Roberts, A.P., Rohling, E.J. and Sagnotti, L., 2003.
1037 Quaternary climatic control of biogenic magnetite production and eolian dust input in cores
1038 from the Mediterranean Sea. *Palaeogeography, Palaeoclimatology, Palaeoecology*, 190,
1039 pp.195-209.
- 1040 Dymond, J., Suess, E., and Lyle, M. (1992). Barium in Deep-Sea Sediment: A Geochemical
1041 Proxy for Paleoproductivity. *Paleoceanography*, 7(2), 163–181.
- 1042 Edgar, K. M., Bohaty, S. M., Coxall, H. K., Bown, P. R., Batenburg, S. J., Lear, C. H.,
1043 Pearson, P. N. (2020). New composite bio- and isotope stratigraphies spanning the
1044 Middle Eocene Climatic Optimum at tropical ODP Site 865 in the Pacific Ocean.
1045 *Journal of Micropalaeontology*, 39, 117–138.
- 1046 Eickmann, B., Hofmann, A., Wille, M., Bui, T. H., Wing, B. A., and Schoenberg, R. (2018).
1047 Isotopic evidence for oxygenated Mesoarchean shallow oceans. *Nature Geoscience*,
1048 11(2), 133–138.
- 1049 Elrod, V. A., Berelson, W. M., Coale, K. H., and Johnson, K. S. (2004). The flux of iron from
1050 continental shelf sediments: A missing source for global budgets. *Geophysical*
1051 *Research Letters*, 31(12).
- 1052 Emiroglu, S., Rey, D., Petersen, N., 2004. Magnetic properties of sediment in the Ria de
1053 Arousa (Spain): dissolution of iron oxides and formation of iron sulphides. *Phys.*
1054 *Chem. Earth* 29, 947-959.
- 1055 Field, M. P., and Sherrell, R. M. (2000). Dissolved and particulate Fe in a hydrothermal
1056 plume at 9°45'N, East Pacific Rise: Slow Fe (II) oxidation kinetics in Pacific plumes.
1057 *Geochimica et Cosmochimica Acta*, 64(4), 619–628.

- 1058 Fioroni, C., Villa, G., Persico, D., Jovane, L. (2015). Middle Eocene-Lower Oligocene
1059 calcareous nannofossil biostratigraphy and paleoceanographic implications from Site
1060 711 (equatorial Indian Ocean). *Marine Micropaleontology*, 118, 50–62.
- 1061 Frierdich, A. J., Beard, B. L., Scherer, M. M., and Johnson, C. M. (2014). Determination of
1062 the Fe(II)_{aq}–magnetite equilibrium iron isotope fractionation factor using the three-
1063 isotope method and a multi-direction approach to equilibrium. *Earth and Planetary
1064 Science Letters*, 391, 77–86.
- 1065 Froelich, P., Klinkhammer, G. P., Bender, M. L., Luedtke, N. A., Heath, G. R., Cullen, D.,
1066 Dauphin, P., Hammond, D., Hartman, B. and Maynard, V. (1979). Early oxidation of
1067 organic matter in pelagic sediments of the eastern equatorial Atlantic: suboxic
1068 diagenesis. *Geochimica et Cosmochimica Acta*, 43(7), 1075–1090.
- 1069 German, C. R., and Elderfield, H. (1990). Application of the Ce anomaly as a paleoredox
1070 indicator: The ground rules. *Paleoceanography*, 5(5), 823–833.
- 1071 German, C. R., Klinkhammer, G. P., Edmond, J. M., Mura, A., and Elderfield, H. (1990).
1072 Hydrothermal scavenging of rare-earth elements in the ocean. *Nature*, 345(6275),
1073 516–518.
- 1074 Giorgioni, M., Jovane, L., Rego, E. S., Rodelli, D., Frontalini, F., Coccioni, R., Rita
1075 Catanzariti and Özcan, E. (2019). Carbon cycle instability and orbital forcing during the
1076 Middle Eocene Climatic Optimum. *Scientific reports*, 9(1), 1-10.
- 1077 Golden, D. C., Ming, D. W., Morris, R. V., Brearley, A. J., Lauer Jr, H. V., Treiman, A. H.,
1078 Zolensky, M. E, Schwandt, C. S., Lofgren, G. E. and McKay, G. A . (2004). Evidence
1079 for exclusively inorganic formation of magnetite in Martian meteorite ALH84001.
1080 *American Mineralogist*, 89(5–6), 681–695.
- 1081 Haley, B. A., Klinkhammer, G. P., and McManus, J. (2004). Rare earth elements in pore
1082 waters of marine sediments. *Geochimica et Cosmochimica Acta*, 68(6), 1265–1279.
- 1083 Heard, A. W., and Dauphas, N. (2020). Constraints on the coevolution of oxic and sulfidic
1084 ocean iron sinks from Archean–Paleoproterozoic iron isotope records. *Geology*, 48(4),
1085 358–362.
- 1086 Hempel, P., and Bohrmann, G. (1990). Carbonate-free sediment components and aspects of
1087 silica diagenesis at Sites 707, 709, and 711 (Leg 115, western Indian Ocean). In
1088 *Proceedings of the Ocean Drilling Program: Scientific Results* (Vol. 115, pp. 677–
1089 698).
- 1090 Henkel, S., Kasten, S., Poulton, S. W., and Staubwasser, M. (2016). Determination of the
1091 stable iron isotopic composition of sequentially leached iron phases in marine
1092 sediments. *Chemical Geology*, 421, 93–102.
- 1093 Hesse, P. P. (1994). Evidence for bacterial palaeoecological origin of mineral magnetic cycles
1094 in oxic and sub-oxic Tasman Sea sediments. *Marine Geology*, 117(1–4), 1–17.
- 1095 Jickells, T. D., and Spokes, L. J. (2001). Atmospheric iron inputs to the oceans. In D. R.
1096 Turner and K. Hunter (Eds.), *The Biogeochemistry of Iron in Seawater* (Vol.
1097 SCOR/IUPAC Series, pp. 85–121). Wiley.
- 1098 Jickells, T. D., An, Z. S., Andersen, K. K., Baker, A. R., Bergametti, G., Brooks, N., Cao, J.
1099 J., Boyd P. W., Duce, R. A., Hunter, K. A., Kawahata, H., Kubilay, N., laRoche,
1100 J., Liss, P. S., Mahowald, N., Prospero, J. M., Ridgwell, A. J., Tegen, I. and Torres, R.

1101 (2005). Global Iron Connections Between Desert Dust, Ocean Biogeochemistry, and
1102 Climate. *Science*, 308(5718), 67–71.

1103 Jimenez-Lopez, C., Romanek, C. S., and Bazylinski, D. A. (2010). Magnetite as a prokaryotic
1104 biomarker: A review. *Journal of Geophysical Research: Biogeosciences*, 115(G2).

1105 Johnson, C., Beard, B., and Weyer, S. (2020). *Iron Geochemistry: An Isotopic Perspective*.
1106 Cham: Springer International Publishing.

1107 Johnson, C. M., Roden, E. E., Welch, S. A., and Beard, B. L. (2005). Experimental
1108 constraints on Fe isotope fractionation during magnetite and Fe carbonate formation
1109 coupled to dissimilatory hydrous ferric oxide reduction. *Geochimica et Cosmochimica*
1110 *Acta*, 69(4), 963–993.

1111 Johnson, C. M., Beard, B. L., Klein, C., Beukes, N. J., and Roden, E. E. (2008a). Iron isotopes
1112 constrain biologic and abiologic processes in banded iron formation genesis.
1113 *Geochimica et Cosmochimica Acta*, 72(1), 151–169.

1114 Johnson, C. M., Beard, B. L., and Roden, E. E. (2008b). The Iron Isotope Fingerprints of
1115 Redox and Biogeochemical Cycling in Modern and Ancient Earth. *Annual Review of*
1116 *Earth and Planetary Sciences*, 36(1), 457–493.

1117 Jovane, L., Florindo, F., Bazylinski, D. A., Lins, U. (2012). Prismatic magnetite
1118 magnetosomes from cultivated *Magnetovibrio blakemorei* strain MV-1: a magnetic
1119 fingerprint in marine sediments? *Environmental Microbiology Reports*, 4, 664–668.

1120 Karlin, R. (1990a). Magnetic mineral diagenesis in suboxic sediments at Bettis Site W-N, NE
1121 Pacific Ocean. *Journal of Geophysical Research: Solid Earth*, 95(B4), 4421–4436.

1122 Karlin, R. (1990b). Magnetite diagenesis in marine sediments from the Oregon continental
1123 margin. *Journal of Geophysical Research: Solid Earth*, 95(B4), 4405–4419.

1124 Klinkhammer, G. P., and Bender, M. L. (1980). The distribution of manganese in the Pacific
1125 Ocean. *Earth and Planetary Science Letters*, 46(3), 361–384.

1126 Klinkhammer, G. P., Elderfield, H., Edmond, J. M., and Mitra, A. (1994). Geochemical
1127 implications of rare earth element patterns in hydrothermal fluids from mid-ocean
1128 ridges. *Geochimica et Cosmochimica Acta*, 58(23), 5105–5113.

1129 Komeili, A. (2012). Molecular mechanisms of compartmentalization and biomineralization in
1130 magnetotactic bacteria. *FEMS Microbiology Reviews*, 36(1), 232–255.

1131 Kopp, R. E., and Kirschvink, J. L. (2008). The identification and biogeochemical
1132 interpretation of fossil magnetotactic bacteria. *Earth-Science Reviews*, 86(1–4), 42–61.

1133 Kostka, J. E., and Luther, G. W. (1994). Partitioning and speciation of solid phase iron in
1134 saltmarsh sediments. *Geochimica et Cosmochimica Acta*, 58(7), 1701–1710.

1135 Kryc, K. A., Murray, R. W., and Murray, D. W. (2003). Elemental fractionation of Si, Al, Ti,
1136 Fe, Ca, Mn, P, and Ba in five marine sedimentary reference materials: results from
1137 sequential extractions. *Analytica Chimica Acta*, 487(1), 117–128.

1138 Kurzweil, F., Wille, M., Gantert, N., Beukes, N. J., and Schoenberg, R. (2016). Manganese
1139 oxide shuttling in pre-GOE oceans – evidence from molybdenum and iron isotopes.
1140 *Earth and Planetary Science Letters*, 452, 69–78.

1141 Lefèvre, C. T., and Bazylinski, D. A. (2013). Ecology, Diversity, and Evolution of
1142 Magnetotactic Bacteria. *Microbiology and Molecular Biology Reviews*, 77(3), 497–
1143 526.

- 1144 Levasseur, S., Frank, M., Hein, J. R., and Halliday, A. N. (2004). The global variation in the
1145 iron isotope composition of marine hydrogenetic ferromanganese deposits:
1146 implications for seawater chemistry? *Earth and Planetary Science Letters*, 224(1–2),
1147 91–105.
- 1148 Lin, W., Paterson, G. A., Zhu, Q., Wang, Y., Kopylova, E., Li, Y., Knight, R., Bazylinski, D.
1149 A., Zhu, R., Kirschvink, J. L. and Pan, Y. (2017). Origin of microbial
1150 biomineralization and magnetotaxis during the Archean. *Proceedings of the National
1151 Academy of Sciences*, 114(9), 2171–2176.
- 1152 Lippert, P. C., and Zachos, J. C. (2007). A biogenic origin for anomalous fine-grained
1153 magnetic material at the Paleocene-Eocene boundary at Wilson Lake, New Jersey.
1154 *Paleoceanography*, 22(4).
- 1155 Luciani, V., Giusberti, L., Agnini, C., Fornaciari, E., Rio, D., Spofforth, D. J. A., and Pälke,
1156 H. (2010). Ecological and evolutionary response of Tethyan planktonic foraminifera to
1157 the middle Eocene climatic optimum (MECO) from the Alano section (NE Italy).
1158 *Palaeogeography, Palaeoclimatology, Palaeoecology*, 292(1–2), 82–95.
- 1159 Mandernack, K. W., Bazylinski, D. A., Shanks, W. C., and Bullen, T. D. (1999). Oxygen and
1160 Iron Isotope Studies of Magnetite Produced by Magnetotactic Bacteria. *Science*,
1161 285(5435), 1892–1896.
- 1162 Marin-Carbonne, J., Rollion-Bard, C., Bekker, A., Rouxel, O., Agangi, A., Cavalazzi, B.,
1163 Wohlgemuth-Ueberwasser C. C., Hofmann A. and McKeegan, K. D. (2014). Coupled
1164 Fe and S isotope variations in pyrite nodules from Archean shale. *Earth and Planetary
1165 Science Letters*, 392, 67-79.
- 1166 Marin Carbonne, J. (2020). Fe isotope composition of Archean sulfides do not record
1167 progressive oxygenation of the ocean. *Geology*, 48(4), 415–416.
- 1168 Martin, J. H., Gordon, M., and Fitzwater, S. E. (1991). The case for iron. *Limnology and
1169 Oceanography*, 36(8), 1793–1802.
- 1170 Martini, E., 1971. Standard tertiary and quaternary calcareous nannoplankton zonation. In:
1171 Farinacci, A. (Ed.), Proc. Second Planktonic Conf., Rome 1970. Tecnoscienza 2, pp.
1172 739–785. [L]
[SEP]
- 1173 Mascarenhas-Pereira, M. B. L., and Nath, B. N. (2010). Selective leaching studies of
1174 sediments from a seamount flank in the Central Indian Basin: Resolving hydrothermal,
1175 volcanogenic and terrigenous sources using major, trace and rare-earth elements.
1176 *Marine Chemistry*, 121(1–4), 49–66.
- 1177 Mcduff, R. E. (1995). Physical dynamics of deep-sea hydrothermal plumes. *GMS*, 91, 357–
1178 368.
- 1179 McKeague, J., and Day, Jh. (1966). Dithionite-and oxalate-extractable Fe and Al as aids in
1180 differentiating various classes of soils. *Canadian Journal of Soil Science*, 46(1), 13–
1181 22.
- 1182 McManus, J., Berelson, W. M., Hammond, D. E., and Klinkhammer, G. P. (1999). Barium
1183 Cycling in the North Pacific: Implications for the Utility of Ba as a Paleoproductivity
1184 and Paleoalkalinity Proxy. *Paleoceanography*, 14(1), 53–61.
- 1185 Merkouriev, S.A. and Sotchevanova, N.A., 2003. Structure and evolution of the Carlsberg
1186 Ridge: Evidence for non-stationary spreading on old and modern spreading centres.
1187 *CURRENT SCIENCE-BANGALORE*-, 85(3), pp.334-338.

- 1188 Moebius, I., Friedrich, O., and Scher, H. D. (2014). Changes in Southern Ocean bottom water
1189 environments associated with the Middle Eocene Climatic Optimum (MECO).
1190 *Palaeogeography, Palaeoclimatology, Palaeoecology*, 405, 16–27.
- 1191 Moebius, I., Friedrich, O., Edgar, K. M., and Sexton, P. F. (2015). Episodes of intensified
1192 biological productivity in the subtropical Atlantic Ocean during the termination of the
1193 Middle Eocene Climatic Optimum (MECO): Intensified Productivity During the
1194 MECO. *Paleoceanography*, 30(8), 1041–1058.
- 1195 Moeller, K., Schoenberg, R., Grenne, T., Thorseth, I. H., Drost, K., and Pedersen, R. B.
1196 (2014). Comparison of iron isotope variations in modern and Ordovician siliceous Fe
1197 oxyhydroxide deposits. *Geochimica et Cosmochimica Acta*, 126, 422–440.
- 1198 Mohamed, K.J., Rey, D., Rubio, B., Dekkers, M.J., Roberts, A.P., Vilas, F., 2011. Onshore–
1199 offshore gradient in reductive early diagenesis in coastal marine sediments of the Ria
1200 de Vigo, Northwest Iberian Peninsula. *Cont. Shelf Res.* 31, 433–447.
- 1201 Moore, J. K., and Braucher, O. (2008). Sedimentary and mineral dust sources of dissolved
1202 iron to the world ocean. *Biogeosciences*, 5(3), 631–656.
- 1203 Nirel, P. M. V., and Morel, F. M. M. (1990). Pitfalls of sequential extractions. *Water*
1204 *Research*, 24(8), 1055–1056.
- 1205 Ohta, A., and Kawabe, I. (2001). REE(III) adsorption onto Mn dioxide (δ -MnO₂) and Fe
1206 oxyhydroxide: Ce(III) oxidation by δ -MnO₂. *Geochimica et Cosmochimica Acta*,
1207 65(5), 695–703.
- 1208 Okada, H., Bukry, D., 1980. Supplementary modification and introduction of code num-
1209 bers to the low-latitude coccolith biostratigraphic zonation (Bukry, 1973, 1975).
1210 *Mar. Micropaleontol.* 5, 321–325. ^[1]_{SEP}
- 1211 Oonk, P. B. H., Tsikos, H., Mason, P. R. D., Henkel, S., Staubwasser, M., Fryer, L., Poulton,
1212 S. W. and Williams, H. M. (2017). Fraction-specific controls on the trace element
1213 distribution in iron formations: Implications for trace metal stable isotope proxies.
1214 *Chemical Geology*, 474, 17–32.
- 1215 Pälike, H., Lyle, M. W., Nishi, H., Raffi, I., Ridgwell, A., Gamage, K., et al. (2012). A
1216 Cenozoic record of the equatorial Pacific carbonate compensation depth. *Nature*,
1217 488(7413), 609–614.
- 1218 Planavsky, N., Rouxel, O., Bekker, A., Shapiro, R., Fralick, P., and Knudsen, A. (2009). Iron-
1219 oxidizing microbial ecosystems thrived in late Paleoproterozoic redox-stratified
1220 oceans. *Earth and Planetary Science Letters*, 286(1–2), 230–242.
- 1221 Planavsky, N., Bekker, A., Rouxel, O. J., Kamber, B., Hofmann, A., Knudsen, A., and Lyons,
1222 T. W. (2010). Rare Earth Element and yttrium compositions of Archean and
1223 Paleoproterozoic Fe formations revisited: New perspectives on the significance and
1224 mechanisms of deposition. *Geochimica et Cosmochimica Acta*, 74(22), 6387–6405.
- 1225 van der Ploeg, R., Selby, D., Cramwinckel, M. J., Li, Y., Bohaty, S. M., Middelburg, J. J., and
1226 Sluijs, A. (2018). Middle Eocene greenhouse warming facilitated by diminished
1227 weathering feedback. *Nature Communications*, 9(1), 2877.
- 1228 Poulton, S. W., and Canfield, D. E. (2005). Development of a sequential extraction procedure
1229 for iron: implications for iron partitioning in continentally derived particulates.
1230 *Chemical Geology*, 214(3–4), 209–221.

- 1231 Raiswell, R., and Canfield, D. E. (2012). The Iron Biogeochemical Cycle Past and Present.
1232 *Geochemical Perspectives*, 1(1), 1–220.
- 1233 Reitz, A., Pfeifer, K., de Lange, G. J., and Klump, J. (2004). Biogenic barium and the detrital
1234 Ba/Al ratio: a comparison of their direct and indirect determination. *Marine Geology*,
1235 204(3), 289–300.
- 1236 Riquier, L., Tribouvillard, N., Averbuch, O., Joachimski, M. M., Racki, G., Devleeschouwer,
1237 X., El Albani, A. and Riboulleau, A. (2005). Chapter 8. Productivity and bottom water
1238 redox conditions at the Frasnian-Famennian boundary on both sides of the Eovariscan
1239 Belt: constraints from trace-element geochemistry. In D. J. Over, J. R. Morrow, and P.
1240 B. Wignall (Eds.), *Developments in Palaeontology and Stratigraphy* (Vol. 20, pp.
1241 199–224).
- 1242 Roberts, A. P. (2015). Magnetic mineral diagenesis. *Earth-Science Reviews*, 151, 1–47.
- 1243 Roberts, A. P., Florindo, F., Villa, G., Chang, L., Jovane, L., Bohaty, S. M., Larrasoana, J. C.,
1244 Heslop, D. and Fitz Gerald, J. D. (2011). Magnetotactic bacterial abundance in pelagic
1245 marine environments is limited by organic carbon flux and availability of dissolved
1246 iron. *Earth and Planetary Science Letters*, 310(3–4), 441–452.
- 1247 Rouxel, O., Shanks III, W. C., Bach, W., and Edwards, K. J. (2008). Integrated Fe-and S-
1248 isotope study of seafloor hydrothermal vents at East Pacific Rise 9–10 N. *Chemical
1249 Geology*, 252(3–4), 214–227.
- 1250 Rouxel, O., Toner, B. M., Manganini, S. J., and German, C. R. (2016). Geochemistry and iron
1251 isotope systematics of hydrothermal plume fall-out at East Pacific Rise 9°50'N.
1252 *Chemical Geology*, 441, 212–234.
- 1253 Rouxel, O. J. (2005). Iron Isotope Constraints on the Archean and Paleoproterozoic Ocean
1254 Redox State. *Science*, 307(5712), 1088–1091.
- 1255 Savian, J. F., Jovane, L., Bohaty, S. M., and Wilson, P. A. (2013). Middle Eocene to early
1256 Oligocene magnetostratigraphy of ODP Hole 711A (Leg 115), western equatorial
1257 Indian Ocean. *Geological Society, London, Special Publications*, 373(1), 97–110.
- 1258 Savian, J. F., Jovane, L., Frontalini, F., Trindade, R. I. F., Coccioni, R., Bohaty, S. M.,
1259 Wilson, P. A., Florindo, F., Roberts, A. P., Catanzariti, R. and Iacoviello, F. (2014).
1260 Enhanced primary productivity and magnetotactic bacterial production in response to
1261 middle Eocene warming in the Neo-Tethys Ocean. *Palaeogeography,
1262 Palaeoclimatology, Palaeoecology*, 414, 32–45.
- 1263 Savian, J. F., Jovane, L., Giorgioni, M., Iacoviello, F., Rodelli, D., Roberts, A. P., Chang, L.,
1264 Florindo, F. and Sprovieri, M. (2016). Environmental magnetic implications of
1265 magnetofossil occurrence during the Middle Eocene Climatic Optimum (MECO) in
1266 pelagic sediments from the equatorial Indian Ocean. *Palaeogeography,
1267 Palaeoclimatology, Palaeoecology*, 441, 212–222.
- 1268 Schoenberg, R., and von Blanckenburg, F. (2005). An assessment of the accuracy of stable Fe
1269 isotope ratio measurements on samples with organic and inorganic matrices by high-
1270 resolution multicollector ICP-MS. *International Journal of Mass Spectrometry*,
1271 242(2–3), 257–272.
- 1272 Schumann, D., Raub, T. D., Kopp, R. E., Guerquin-Kern, J.-L., Wu, T.-D., Rouiller, I.,
1273 Smirnov, A. V., Sears, S. K., Lücken, U., Tikoo, S. M., Hesse, R., Kirschvink, J. L.
1274 and Vali, H. (2008). Gigantism in unique biogenic magnetite at the Paleocene-Eocene

1275 Thermal Maximum. *Proceedings of the National Academy of Sciences*, 105(46),
1276 17648–17653.

1277 Severmann, S., Johnson, C. M., Beard, B. L., German, C. R., Edmonds, H. N., Chiba, H., and
1278 Green, D. R. H. (2004). The effect of plume processes on the Fe isotope composition
1279 of hydrothermally derived Fe in the deep ocean as inferred from the Rainbow vent
1280 site, Mid-Atlantic Ridge, 36°14'N. *Earth and Planetary Science Letters*, 225(1), 63–
1281 76.

1282 Severmann, S., Johnson, C. M., Beard, B. L., and McManus, J. (2006). The effect of early
1283 diagenesis on the Fe isotope compositions of porewaters and authigenic minerals in
1284 continental margin sediments. *Geochimica et Cosmochimica Acta*, 70(8), 2006–2022.

1285 Sharma, M., Polizzotto, M., and Anbar, A. D. (2001). Iron isotopes in hot springs along the
1286 Juan de Fuca Ridge. *Earth and Planetary Science Letters*, 194(1), 39–51.

1287 Simmons, G.R., 1990. Subsidence history of basement sites and sites along a carbonate
1288 dissolution profile. *Proceedings of the ODP (Ocean Drilling Program), Scientific Results*,
1289 *Leg 115, College Station, TX*, pp.123-126.

1290 Slotznick, S.P., Sperling, E.A., Tosca, N.J., Miller, A.J., Clayton, K.E., van Helmond,
1291 N.A.G.M., Slomp, C.P. and Swanson-Hysell, N.L., 2020. Unraveling the mineralogical
1292 complexity of sediment iron speciation using sequential extractions. *Geochemistry*,
1293 *Geophysics, Geosystems*, 21(2).

1294 Sluijs, A., Zeebe, R. E., Bijl, P. K., and Bohaty, S. M. (2013). A middle Eocene carbon cycle
1295 conundrum. *Nature Geoscience*, 6(6), 429–434.

1296 Spofforth, D. J. A., Agnini, C., Pälike, H., Rio, D., Fornaciari, E., Giusberti, L., Luciani, V.,
1297 Lanci, L. and Muttoni, G. (2010). Organic carbon burial following the middle Eocene
1298 climatic optimum in the central western Tethys. *Paleoceanography*, 25(3).

1299 Staubwasser, M., von Blanckenburg, F., and Schoenberg, R. (2006). Iron isotopes in the early
1300 marine diagenetic iron cycle. *Geology*, 34(8), 629.

1301 Taylor, S. R., and McLennan, S. M. (1995). The geochemical evolution of the continental
1302 crust. *Reviews of Geophysics*, 33(2), 241–265.

1303 Tessier, Andre., and Campbell, P. G. C. (1988). Comments on the testing of the accuracy of
1304 an extraction procedure for determining the partitioning of trace metals in sediments.
1305 *Analytical Chemistry*, 60(14), 1475–1476.

1306 Thomas-Keprta, K. L., Bazylinski, D. A., Kirschvink, J. L., Clemett, S. J., McKay, D. S.,
1307 Wentworth, S. J., Vali, H., Gibson Jr, E. K. and Romanek, C. S. (2000). Elongated
1308 prismatic magnetite crystals in ALH84001 carbonate globules: Potential Martian
1309 magnetofossils. *Geochimica et Cosmochimica Acta*, 64(23), 4049–4081.

1310 Toffanin, F., Agnini, C., Fornaciari, E., Rio, D., Giusberti, L., Luciani, V., Spofforth, D. J. A
1311 and Pälike, H. (2011). Changes in calcareous nannofossil assemblages during the
1312 Middle Eocene Climatic Optimum: Clues from the central-western Tethys (Alano
1313 section, NE Italy). *Marine Micropaleontology*, 81(1–2), 22–31.

1314 Torfstein, A., Winckler, G., and Tripathi, A. (2010). Productivity feedback did not terminate
1315 the Paleocene-Eocene Thermal Maximum (PETM). *Clim. Past*, 8.

1316 Tribouillard, N., Riboulleau, A., Lyons, T., and Baudin, F. (2004). Enhanced trapping of
1317 molybdenum by sulfurized marine organic matter of marine origin in Mesozoic
1318 limestones and shales. *Chemical Geology*, 213(4), 385–401.

- 1319 Tribovillard, N., Algeo, T. J., Lyons, T., and Riboulleau, A. (2006). Trace metals as
1320 paleoredox and paleoproductivity proxies: An update. *Chemical Geology*, 232(1–2),
1321 12–32.
- 1322 Vali, H., and Kirschvink, J. L. (1989). Magnetofossil dissolution in a palaeomagnetically
1323 unstable deep-sea sediment. *Nature*, 339(6221), 203–206.
- 1324 Villa, G., Fioroni, C., Persico, D., Roberts, A. P., and Florindo, F. (2014). Middle Eocene to
1325 Late Oligocene Antarctic glaciation/deglaciation and Southern Ocean productivity.
1326 *Paleoceanography*, 29(3), 223–237.
- 1327 Weyer, S., and Schwieters, J. B. (2003). High precision Fe isotope measurements with high
1328 mass resolution MC-ICPMS. *International Journal of Mass Spectrometry*, 226(3),
1329 355–368.
- 1330 Winter, B. L., Johnson, C. M., and Clark, D. L. (1997). Geochemical constraints on the
1331 formation of Late Cenozoic ferromanganese micronodules from the central Arctic
1332 Ocean. *Marine Geology*, 138(1–2), 149–169.
- 1333 Witkowski, J., Bohaty, S. M., McCartney, K., and Harwood, D. M. (2012). Enhanced
1334 siliceous plankton productivity in response to middle Eocene warming at Southern
1335 Ocean ODP Sites 748 and 749. *Palaeogeography, Palaeoclimatology, Palaeoecology*,
1336 326–328, 78–94.
- 1337 Witkowski, J., Bohaty, S. M., Edgar, K. M., and Harwood, D. M. (2014). Rapid fluctuations
1338 in mid-latitude siliceous plankton production during the Middle Eocene Climatic
1339 Optimum (ODP Site 1051, western North Atlantic). *Marine Micropaleontology*, 106,
1340 110–129.
- 1341 Yamazaki, T., Abdeldayem, A. L., and Ikehara, K. (2003). Rock-magnetic changes with
1342 reduction diagenesis in Japan Sea sediments and preservation of geomagnetic secular
1343 variation in inclination during the last 30,000 years. *Earth, Planets and Space*, 55(6),
1344 327–340.
- 1345 Young, E. D., Galy, A., and Nagahara, H. (2002). Kinetic and equilibrium mass-dependent
1346 isotope fractionation laws in nature and their geochemical and cosmochemical
1347 significance. *Geochimica et Cosmochimica Acta*, 66(6), 1095–1104.

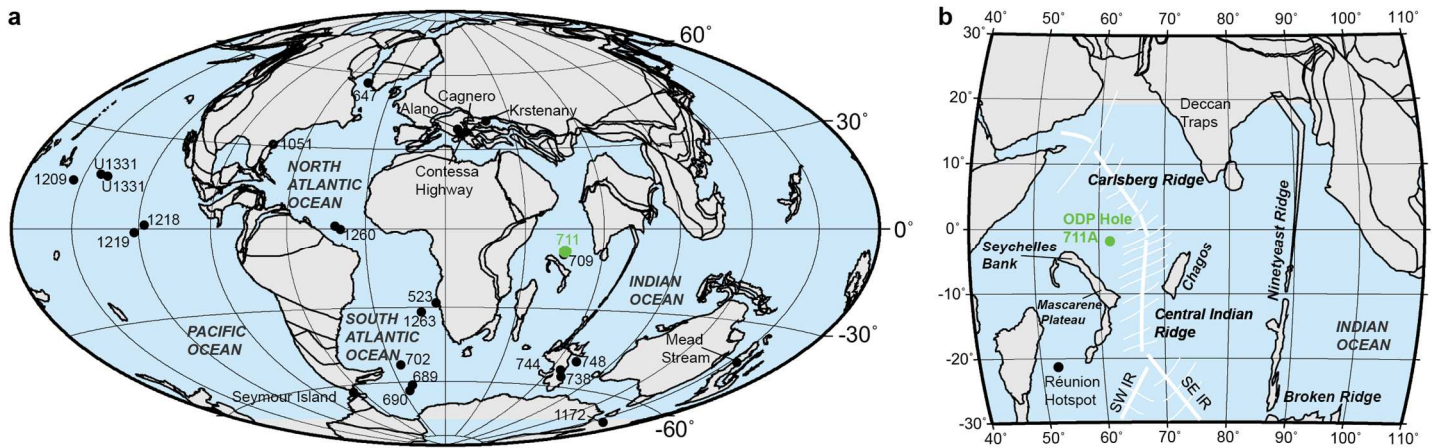


Fig. 1. Map showing paleo-position on a 40 Ma reconstruction (a) and present position (b) of ODP Site 711A (green dot) and other sites where the MECO event has been reported (black dots on left figure) (modified from Savian et al., 2016). The maps were plotted using a paleogeographic reconstruction created using the Ocean Drilling Stratigraphic Network (GEOMAR, Kiel, Germany) website. Considering a half spreading rate of about 1.5 cm/yr since ~ 45 Ma (Merkouriev and Sotchevanova, 2003), ODP Site 711A would have lied less than 100 km away from the central Indian and Carlsberg ridges at the time of the MECO event (schematically represented in white here; SW IR and SE IR on right figure stand for South West and South East Indian Ridges, respectively).

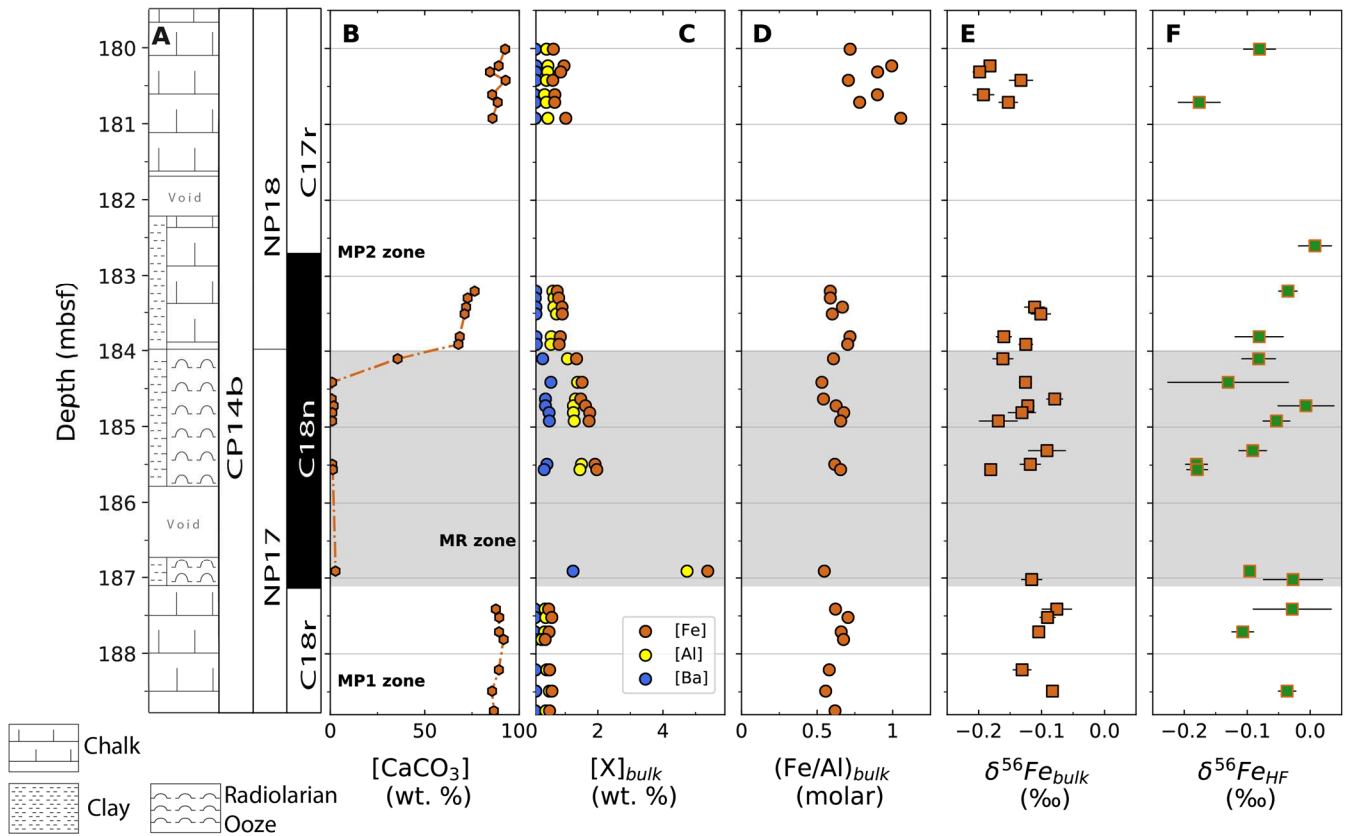


Fig. 2. Stratigraphic variations of selected geochemical indicators in the bulk sediment and HF fraction (see subscript bulk or HF on axis title). (A) From left to right: lithological log (modified after Backman et al., 1988), calcareous nannofossil zonation (Okada and Bukry, 1980; Martini, 1971) and magnetic polarity sequence (modified after Savian et al., 2016). (B) Calcite concentrations, which approach 0 in MR zone, indicating that Hole 711A lied below the CCD at this time. (C) Fe and Al concentrations. (D) Fe/Al molar ratios. Iron isotope compositions in (E) bulk sediment and (F) HF fraction. Both $\delta^{56}\text{Fe}$ values exhibit similar and restricted values and no clear stratigraphic trend. Error bars correspond to 1σ values. Following Savian et al. (2013), the MECO's peak (~40 Ma) would occur at the start of MR zone.

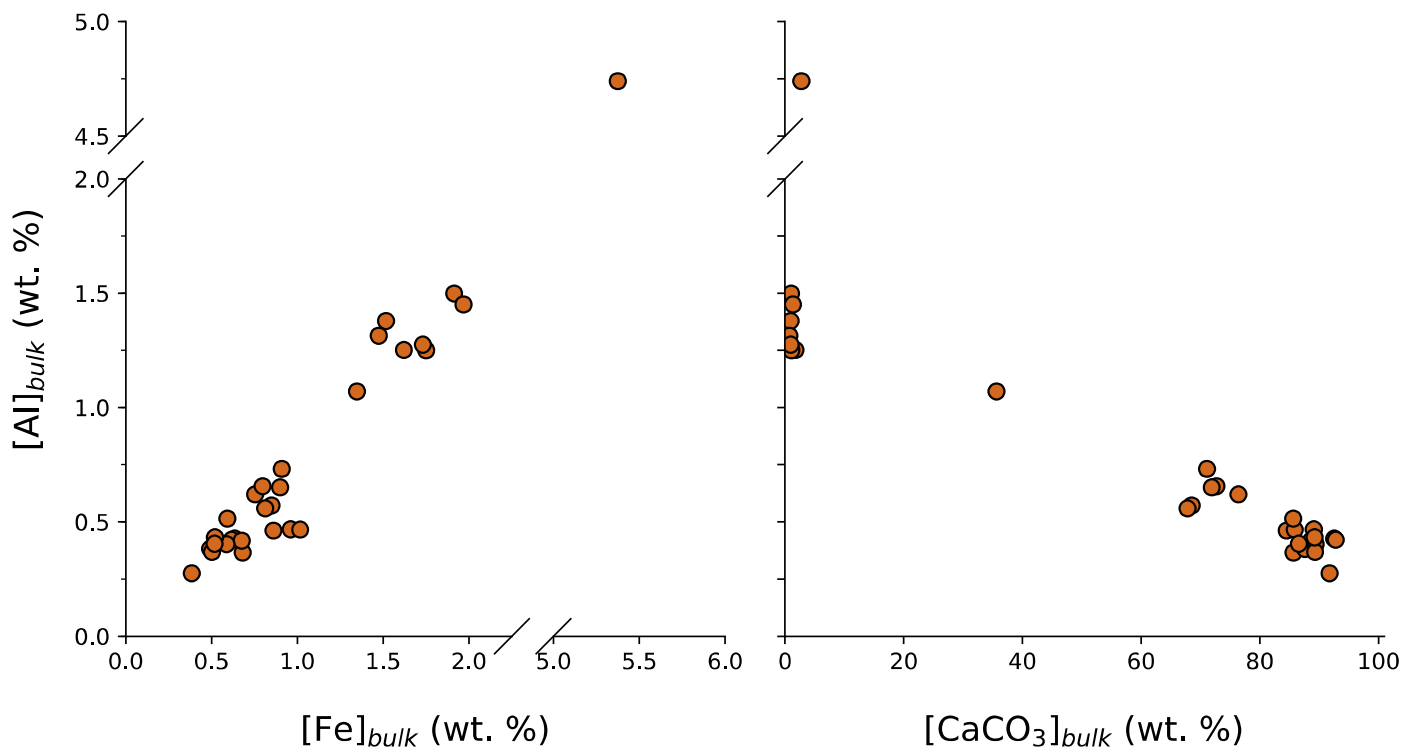


Fig. 3. Correlations between bulk aluminum, iron and calcite concentrations in ODP Site 711A sediments. Al and Fe concentrations axes were broken for better visibility of sample '186.91 mbsf', which shows a strong enrichment in Al and Fe relative to other samples.

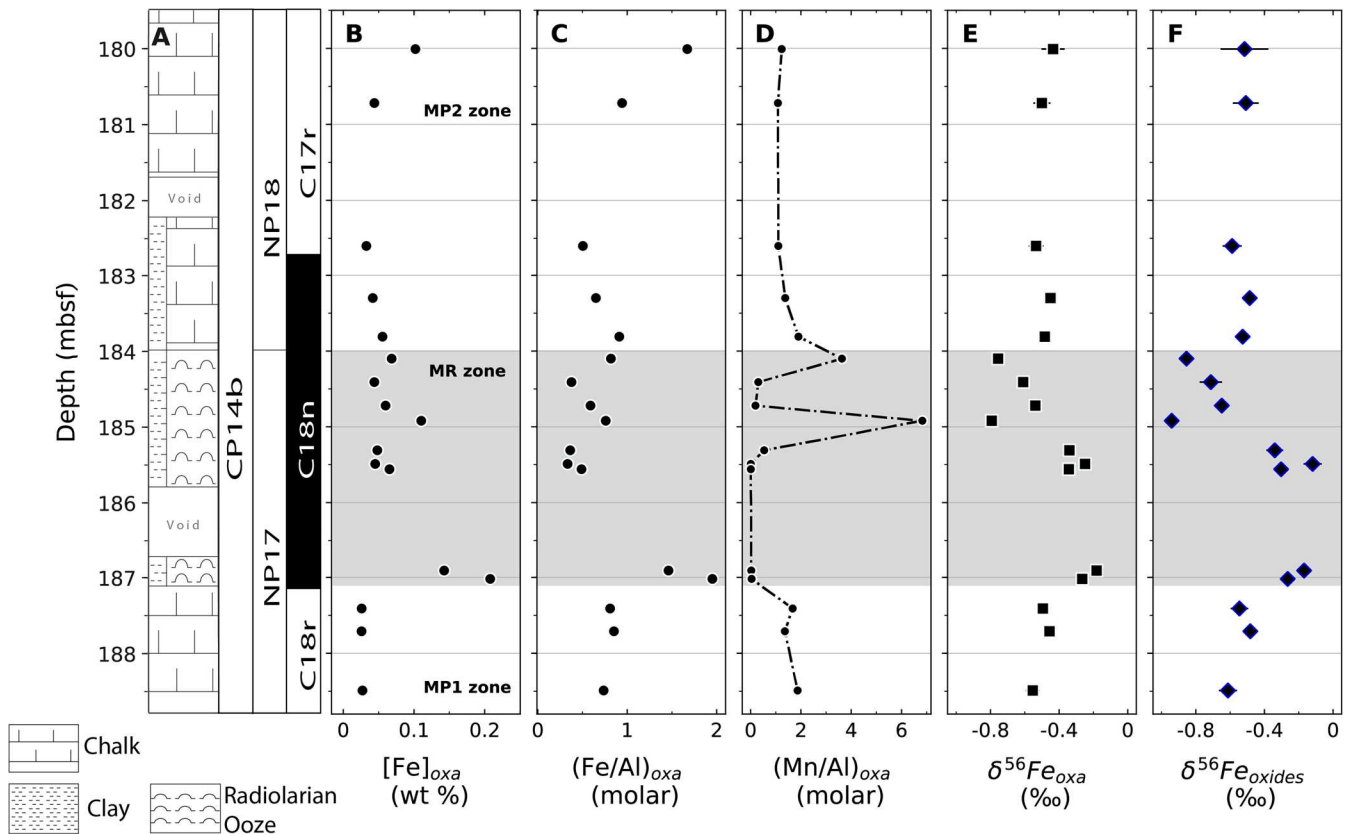


Fig. 4. Stratigraphic variations of selected geochemical indicators in the oxalate fraction. (A) From left to right: lithological log (modified after Backman et al., 1988), calcareous nannofossil zonation (Okada and Bukry, 1980; Martini, 1971) and magnetic polarity sequence (modified after Savian et al. 2016). (B) Fe concentrations, (C) Fe/Al and (D) Mn/Al molar ratios. (E) $\delta^{56}Fe_{oxa}$ values measured in the oxalate fraction. (F) $\delta^{56}Fe_{oxides}$ values correspond to $\delta^{56}Fe_{oxa}$ values corrected from silicate-Fe contaminations arising from the oxalic acid ammonium oxalate (OA-AO) extraction step (see Discussion in 5.1). $\delta^{56}Fe_{oxides}$ exhibit a slightly broader range of variations and more negative absolute values. Error bars correspond to 1σ values. Following Savian et al. (2013), the MECO's peak (~40 Ma) would occur at the start MR zone.

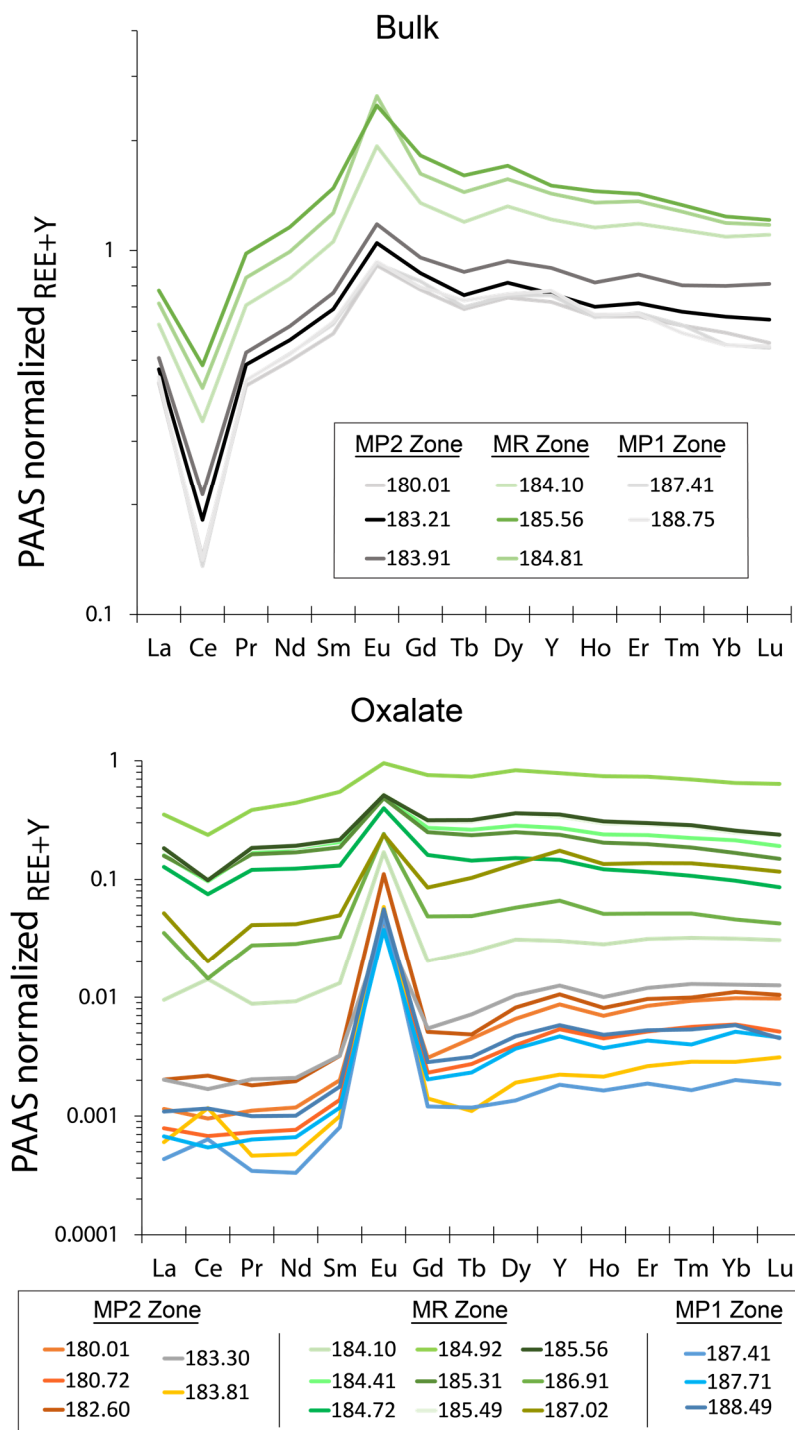


Fig. 5. Shale-normalized REE+Y patterns of the bulk sediments (top) and oxalate fraction (bottom), shown in a logarithmic scale. All REE and Y concentrations were normalized to Post Archean Australian Shale (PAAS; Taylor and McLennan, 1995). Green curves correspond to samples from MR zone.

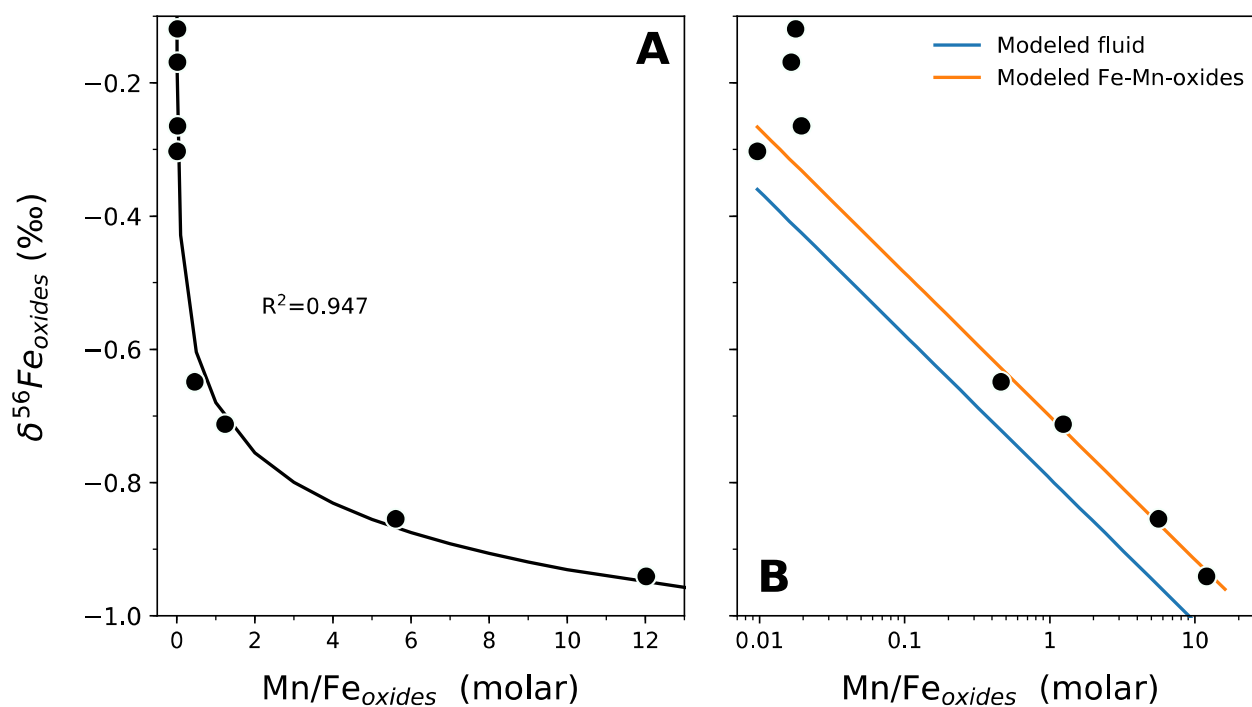


Fig. 6. Evolution of $\delta^{56}\text{Fe}$ versus Mn/Fe molar ratio in MR zone samples for the “oxide fraction” (*i.e.* silicate-corrected oxalate fraction). (A) Solid black line represents the logarithmic linear regression curve fitting the data ($y = -1.109 \ln(x) - 0.6798$, correlation coefficient $R^2 = 0.947$). (B) Comparison between the fluid (blue) and Fe-Mn oxides (orange) isotopic composition modeled with Rayleigh fractionation equations and the “oxide fraction” data. The modeled $\delta^{56}\text{Fe}$ of Fe-Mn oxides (orange) represents Fe included in magnetites and possibly Mn-oxides forming in diverse redox conditions (see main text for details). The calculated initial fluid composition and fractionation factor are 0.36 ‰ and 0.09 ‰, respectively. The four Mn-depleted samples (187.02, 186.91, 185.46 and 185.49 mbsf) have similar Mn/Fe lying close to 0 but variable $\delta^{56}\text{Fe}$ and thus cannot be perfectly fitted. Relative to the modeled fluid, at similar Mn/Fe ratios, they express a fractionation ranging from ~ 0.06 to 0.30 ‰.

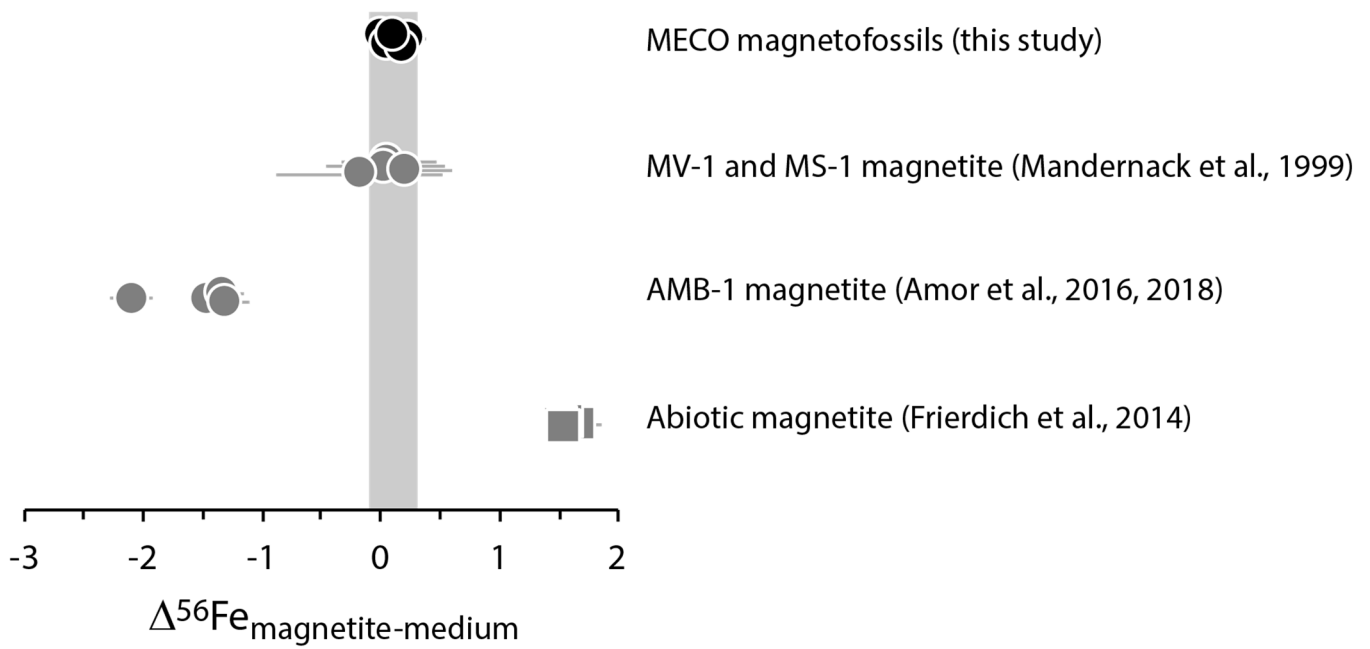


Fig. 7. Comparison of Fe isotope fractionations ($\Delta^{56}\text{Fe}$) recorded in magnetofossils (this study) and magnetites formed experimentally by various MTB strains (MV-1, MS-1, AMB-1) and abiotic pathways. $\Delta^{56}\text{Fe}$ (in ‰) is defined as the difference in $\delta^{56}\text{Fe}$ values between magnetite crystals and dissolved Fe of the solution they precipitated from. Note that isotopic fractionation determined in our study has small absolute values, close to those of Mandernack et al. (1999), but is clearly distinguishable from that recorded by abiotic magnetite (Friedrich et al., 2014). All error bars of the present data are smaller than symbols size.

Table 1

Selected major and trace element concentrations (in weight percent), normalized to aluminum or iron (as molar ratios) and cerium and europium anomalies (Ce* and Eu*, respectively) for the bulk, oxalate and HF fractions.

Sample	Fraction	Zone	Depth (mbsf*)	CaCO ₃	Fe	Al	Mn	Ba	Normalized to Al			Eu*	Ce*	
									Fe/Al	Mn/Al	Ba/Al			
				(wt. %)				(molar)						
C19 S6 10	<i>Bulk</i>	C	180.01	92.5	0.63	0.43	0.09	0.08	0.72	0.20	0.04	0.14	1.5	0.3
C19 S6 80.5	<i>Bulk</i>	C	180.72	88.6	0.68	0.42	0.09	0.09	0.78	0.22	0.04	0.14	1.5	0.3
C20 S1 50	<i>Bulk</i>	C	182.60											
C20 S1 110	<i>Bulk</i>	C	183.20	72.7	0.80	0.66	0.14	0.08	0.59	0.21	0.02	0.17	1.4	0.4
C20 S2 20	<i>Bulk</i>	C	183.81	68.5	0.85	0.57	0.17	0.10	0.72	0.31	0.04	0.21	1.5	0.4
C20 S2 50	<i>Bulk</i>	B	184.10	35.6	1.35	1.07	0.39	0.31	0.61	0.36	0.06	0.29	1.8	0.5
C20 S2 80	<i>Bulk</i>	B	184.41	0.9	1.52	1.38	0.08	0.56	0.53	0.06	0.08	0.05	2.2	0.6
C20 S2 111.5	<i>Bulk</i>	B	184.72	1.8	1.62	1.25	0.05	0.39	0.63	0.04	0.06	0.03	1.9	0.6
C20 S2 131	<i>Bulk</i>	B	184.92	0.9	1.73	1.28	1.26	0.51	0.66	0.99	0.08	0.74	2.0	0.6
C20 S3 20	<i>Bulk</i>	B	185.31											
C20 S3 38	<i>Bulk</i>	B	185.49	1.0	1.91	1.50	0.02	0.44	0.62	0.01	0.06	0.01	1.8	0.6
C20 S3 45	<i>Bulk</i>	B	185.56	1.3	1.97	1.45	0.01	0.35	0.66	0.01	0.05	0.01	1.7	0.6
C20 S4 31	<i>Bulk</i>	B	186.91	2.7	5.37	4.74	0.05	1.24	0.55	0.01	0.05	0.01	1.8	0.5
C20 S4 40	<i>Bulk</i>	B	187.02											
C20 S4 80.5	<i>Bulk</i>	A	187.41	87.6	0.49	0.38	0.09	0.06	0.62	0.24	0.03	0.19	1.4	0.3
C20 S4 110	<i>Bulk</i>	A	187.71	89.3	0.50	0.37	0.07	0.07	0.66	0.20	0.04	0.15	1.4	0.3
C20 S5 38	<i>Bulk</i>	A	188.49	85.6	0.59	0.51	0.11	0.10	0.56	0.21	0.04	0.18	1.5	0.3
C19 S6 10	<i>Oxalate</i>	C	180.01		0.10	0.03	0.07	0.01	1.67	1.24	0.09	0.74	14.7	0.8
C19 S6 80.5	<i>Oxalate</i>	C	180.72		0.04	0.02	0.05	0.02	0.94	1.09	0.14	1.15	27.2	0.9
C20 S1 50	<i>Oxalate</i>	C	182.60		0.03	0.03	0.07	0.04	0.50	1.10	0.22	2.18	29.8	1.1
C20 S1 110	<i>Oxalate</i>	C	183.20		0.04	0.03	0.09	0.01	0.65	1.38	0.07	2.12	8.7	0.8
C20 S2 20	<i>Oxalate</i>	C	183.81		0.06	0.03	0.11	0.02	0.91	1.90	0.13	2.09	57.4	2.2
C20 S2 50	<i>Oxalate</i>	B	184.10		0.07	0.04	0.30	0.05	0.82	3.63	0.25	4.44	10.1	1.6
C20 S2 80	<i>Oxalate</i>	B	184.41		0.04	0.06	0.03	0.08	0.38	0.30	0.28	0.81	2.2	0.6
C20 S2 111.5	<i>Oxalate</i>	B	184.72		0.06	0.05	0.02	0.09	0.59	0.19	0.36	0.33	3.0	0.6
C20 S2 131	<i>Oxalate</i>	B	184.92		0.11	0.07	0.97	0.09	0.76	6.83	0.26	8.99	1.6	0.6
C20 S3 20	<i>Oxalate</i>	B	185.31		0.05	0.06	0.07	0.09	0.36	0.54	0.28	1.48	2.4	0.6

C20 S3 38	<i>Oxalate</i>	B	185.49	0.05	0.07	0.00	0.08	0.33	0.01	0.25	0.02	2.2	0.6
C20 S3 45	<i>Oxalate</i>	B	185.56	0.07	0.06	0.00	0.08	0.49	0.01	0.24	0.02	2.1	0.5
C20 S4 31	<i>Oxalate</i>	B	186.91	0.14	0.05	0.00	0.07	1.46	0.03	0.28	0.02	6.4	0.5
C20 S4 40	<i>Oxalate</i>	B	187.02	0.21	0.05	0.00	0.06	1.95	0.04	0.22	0.02	3.6	0.4
C20 S4 80.5	<i>Oxalate</i>	A	187.41	0.03	0.02	0.05	0.02	0.81	1.67	0.22	2.07	54.8	1.6
C20 S4 110	<i>Oxalate</i>	A	187.71	0.03	0.01	0.04	0.01	0.85	1.36	0.17	1.60	24.3	0.8
C20 S5 38	<i>Oxalate</i>	A	188.49	0.03	0.02	0.07	0.02	0.74	1.87	0.20	2.54	25.4	1.1
C19 S6 10	<i>HF</i>	C	180.01	0.72	0.40	0.03	0.04	0.88	0.04	0.02	0.04	2.4	0.7
C19 S6 80.5	<i>HF</i>	C	180.72	0.48	0.33	0.02	0.03	0.70	0.02	0.02	0.03	3.9	0.9
C20 S1 50	<i>HF</i>	C	182.60	0.71	0.86	0.02	0.05	0.40	0.01	0.01	0.02	3.6	1.0
C20 S1 110	<i>HF</i>	C	183.20	0.56	0.55	0.02	0.05	0.50	0.01	0.02	0.03	3.0	0.7
C20 S2 20	<i>HF</i>	C	183.81	0.66	0.50	0.02	0.07	0.64	0.02	0.03	0.03	3.3	0.7
C20 S2 50	<i>HF</i>	B	184.10	0.99	0.84	0.02	0.21	0.57	0.01	0.05	0.03	9.9	1.3
C20 S2 80	<i>HF</i>	B	184.41	1.19	1.16	0.02	0.44	0.50	0.01	0.07	0.01	6.3	0.6
C20 S2 111.5	<i>HF</i>	B	184.72	1.31	1.07	0.02	0.24	0.59	0.01	0.04	0.01	3.4	0.6
C20 S2 131	<i>HF</i>	B	184.92	1.32	1.06	0.03	0.38	0.60	0.01	0.07	0.02	5.6	0.6
C20 S3 20	<i>HF</i>	B	185.31	1.40	1.15	0.02	0.32	0.59	0.01	0.05	0.02	4.1	0.6
C20 S3 38	<i>HF</i>	B	185.49	1.37	1.22	0.01	0.37	0.54	0.00	0.06	0.01	4.3	0.6
C20 S3 45	<i>HF</i>	B	185.56	1.54	1.30	0.01	0.29	0.57	0.00	0.04	0.01	3.4	0.6
C20 S4 31	<i>HF</i>	B	186.91	4.42	4.50	0.04	0.97	0.48	0.00	0.04	0.01	2.1	0.5
C20 S4 40	<i>HF</i>	B	187.02	3.99	4.11	0.03	1.19	0.47	0.00	0.06	0.01	2.4	0.5
C20 S4 80.5	<i>HF</i>	A	187.41	0.37	0.31	0.01	0.02	0.57	0.02	0.01	0.03	5.0	1.2
C20 S4 110	<i>HF</i>	A	187.71	0.39	0.31	0.01	0.02	0.61	0.01	0.01	0.02	5.2	1.1
C20 S5 38	<i>HF</i>	A	188.49	0.47	0.43	0.01	0.04	0.53	0.01	0.02	0.03	6.4	1.1

* mbsf: meters below seafloor.

Table 2.

Iron isotope compositions in the bulk, HF, and oxalate fractions, as well as in the silicate-corrected- oxalate fraction ('oxides'), expressed in permil (‰). $\delta^{56}\text{Fe}_{\text{oxa}}$ represents the average of duplicate measurements (including full chemical treatment). Errors are expressed as 2 standard deviations (SD) in permil.

Sample	Zone	Depth (mbsf*)	$\delta^{56}\text{Fe}_{\text{bulk}}$ (‰)	2 SD (‰)	$\delta^{56}\text{Fe}_{\text{HF}}$ (‰)	2 SD (‰)	$\delta^{56}\text{Fe}_{\text{oxa}}$ (‰)	2 SD (‰)	$\delta^{56}\text{Fe}_{\text{oxides}}$ (‰)	2 SD (‰)
C19 S6 10	C	180.01			-0.08	0.05	-0.44	0.14	-0.52	0.28
C19 S6 80.5	C	180.72	-0.15	0.03	-0.18	0.07	-0.50	0.10	-0.53	0.17
C20 S1 50	C	182.60			0.01	0.05	-0.53	0.09	-0.59	0.11
C20 S1 110	C	183.20			-0.04	0.03	-0.45	0.05	-0.49	0.07
C20 S2 20	C	183.81	-0.16	0.03	-0.08	0.08	-0.48	0.05	-0.53	0.08
C20 S2 50	B	184.10	-0.16	0.03	-0.08	0.05	-0.76	0.04	-0.85	0.06
C20 S2 80	B	184.41	-0.13	0.02	-0.13	0.19	-0.61	0.03	-0.71	0.13
C20 S2 111.5	B	184.72	-0.12	0.02	-0.01	0.09	-0.54	0.03	-0.65	0.07
C20 S2 131	B	184.92	-0.17	0.06	-0.05	0.04	-0.79	0.04	-0.94	0.07
C20 S3 20	B	185.31	-0.09	0.06	-0.09	0.05	-0.34	0.03	-0.34	0.10
C20 S3 38	B	185.49	-0.12	0.03	-0.18	0.04	-0.25	0.05	-0.12	0.11
C20 S3 45	B	185.56	-0.18	0.01	-0.18	0.03	-0.34	0.04	-0.30	0.08
C20 S4 31	B	186.91			-0.10	0.01	-0.18	0.04	-0.17	0.04
C20 S4 40	B	187.02	-0.12	0.03	-0.03	0.10	-0.27	0.05	-0.26	0.05
C20 S4 80.5	A	187.41	-0.08	0.05	-0.03	0.13	-0.49	0.06	-0.55	0.10
C20 S4 110	A	187.71	-0.10	0.02	-0.11	0.04	-0.46	0.04	-0.48	0.07
C20 S5 38	A	188.49	-0.08	0.02	-0.04	0.03	-0.55	0.08	-0.61	0.11

* mbsf: meters below seafloor.